

Disentangling Rich Dynamics from Feature Learning: A Framework for Independent Measurements

Yoonsoo Nam^a, Nayara Fonseca^a, Seok Hyeong Lee^b, Chris Mingard^{a,c}, Niclas Göring^a, Ouns El Harzli^d, Abdurrahman Hadi Erturk^a, Soufiane Hayou^e, and Ard A. Louis^a

^aRudolf Peierls Centre for Theoretical Physics, University of Oxford

^bCenter for Quantum Structures in Modules and Spaces, Seoul National University

^cPhysical and Theoretical Chemistry Laboratory, University of Oxford

^dDepartment of Computer Science, University of Oxford

^eSimons Institute for the Theory of Computing, UC Berkeley

Abstract

In machine learning, it is widely believed that dynamic feature transformation (the rich regime) enhances predictive performance. However, this link does not always hold, and existing richness measures rely on correlated factors — such as performance or parameter norms — which can complicate the analysis of feature learning. We introduce (1) a measure that quantifies the rich regime independently of performance, and (2) interpretable feature metrics for visualization. Leveraging low-rank bias, our approach generalizes neural collapse metrics and captures lazy-to-rich transitions (e.g., grokking) without relying on performance as a proxy. We reveal how batch normalization and training set size influence lazy/rich dynamics for VGG16 and ResNet18 on CIFAR-10/100, opening avenues for better understanding feature learning.

1 Introduction

In machine learning, feature learning is often viewed through two complementary perspectives: improvement of representations and non-linear training dynamics. The *representation perspective* emphasizes feature quality — how well it supports downstream tasks like classification and promotes generalization [1]. The *dynamics perspective* — often called rich regime in *rich versus lazy training* [2] — concerns the dynamic transformation of features beyond linear models. While dynamical richness frequently correlates with representation usefulness, rich dynamics reflect a preference (inductive bias) toward certain solutions, without necessarily benefiting all tasks [3]. For example, dynamic feature learning can impair the performance on an image classification task (Fig. 1).

The representation perspective of feature learning — central to deep learning’s success — remains poorly understood. However, its dynamic aspects, often shaped in practice by initialization and optimization, are well understood in the context of layerwise linear models (e.g., linear networks). Greedy dynamics with low-rank biases [4, 5] explain neural collapse [6] in vision tasks; delayed saturation dynamics [7] have been linked to emergence [8] and scaling laws [9] in large language models; and initialization-dependent dynamics [10–13] offer insights into grokking [14] in arithmetic tasks (see Nam et al. [13] for a comprehensive overview).

To better understand the link between rich dynamics and representation improvement, we need independent metrics for dynamics and representations. However, existing dynamics metrics, often designed for purposes beyond practical richness measurement, can conflate learning dynamics with factors such as representation quality, labels, or the initial kernel.

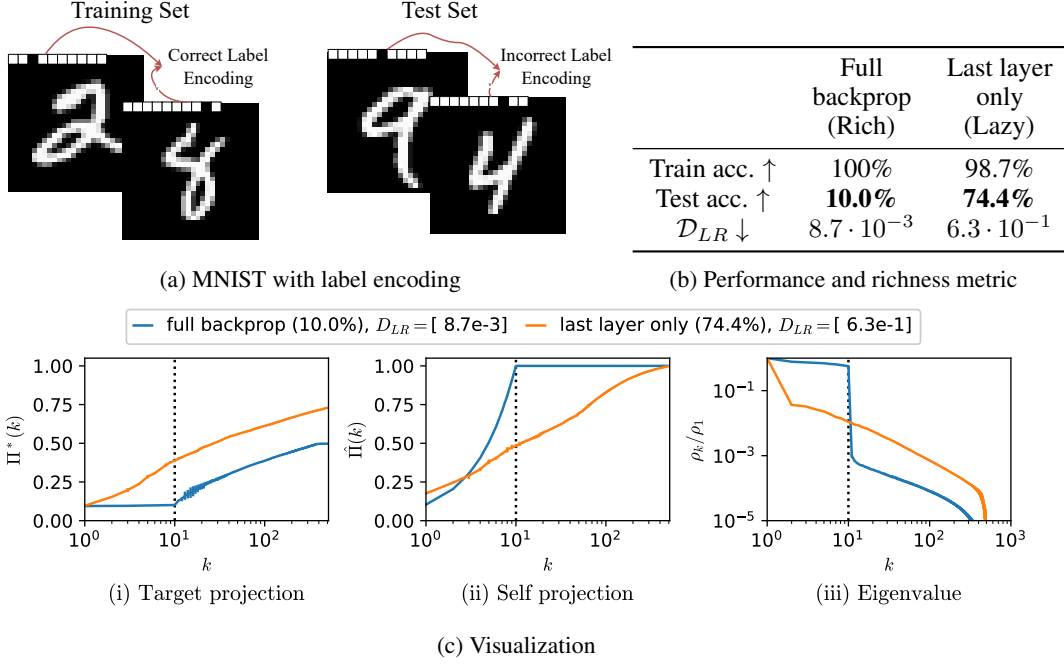


Figure 1: **Rich dynamics \neq better generalization.** We trained a 4-layer MLP on label-encoded MNIST. **(a):** The first 10 pixels are encoded with true labels in training and random labels in testing; both the encoding and the image serve as valid features for training. **(b):** A full backpropagation model (*rich*) biases toward the encodings and generalizes poorly, while a last-layer-only-trained model (*lazy*) relies on the full image and generalizes better. Our low-rank-based metric \mathcal{D}_{LR} (Eq. (4)) quantifies the dynamical richness ($\mathcal{D}_{LR} \in [0, 1]$ where 0 is richest). **(c):** Visualization framework (Eq. (5)): (i) Cumulative contribution of last-layer features in spanning the target function $\Pi^*(k)$ — top 10 features are irrelevant in the rich model. (ii) Contribution to the learned function $\hat{\Pi}(k)$ — the rich model uses only the top 10 features, while the lazy model uses all. (iii) Relative feature norms ρ_k/ρ_1 — rich model concentrates on the top 10; lazy model decays more gradually. Test accuracies and \mathcal{D}_{LR} values are shown in parentheses and square brackets, respectively. See Section 3.2 for details, and Appendix C for background and motivation.

In this paper, we propose a principled metric for dynamical richness that (1) generalizes neural collapse, (2) requires no access to labels or performance, and (3) operates in function space. We further introduce visualization methods that track feature quality, usage, and intensity throughout training. These tools reveal lazy-to-rich transitions (e.g., target downscaling [2, 3] and grokking) without referencing performance and help uncover new patterns, such as the effects of batch normalization and dataset size on rich dynamics. Together, they offer practical tools and conceptual clarity toward understanding feature learning.

Contributions:

- We propose a metric for dynamical richness independent of representational quality (Eq. (4)) and formally show it recovers neural collapse as a special case (Propositions 1 and 2).
- We introduce a visualization framework that disentangles feature quality and dynamical richness (Section 3.2), offering interpretable diagnostics for analyzing training dynamics.
- Using this framework, we reveal known lazy-to-rich transitions without referencing performance. For example, it separately visualizes the representation improvement and lazy-to-rich transition in grokking (Fig. 4) and target downscaling (Fig. 2).
- We reveal new empirical patterns, including a correlation between batch normalization and dynamical richness in VGG16 trained on CIFAR-100 and a correlation between feature quality and intensity in ResNet18 on CIFAR-100.

2 Set up and Background

For analytical tractability, we use MSE loss and supervised settings — e.g., balanced C -way classification or regression with scalar output — where target function entries are orthogonal and isotropic.

Notations. For the input space \mathcal{X} , we train on n samples from q , the underlying true distribution on the input space \mathcal{X} . The width of the last layer (or the linear model) is p . The dimension of the output function (and the output of neural network) is C . Denote \hat{f} and f^* as the learned function (at any point in training) and the target function, respectively. We use bra-ket notation $\langle f|g \rangle := \mathbf{E}_{x \sim q}[f(x)g(x)]$ to mean the inner product over the input distribution (Appendix B). See Appendix A for a **glossary**.

Empirical details. Full experimental details and statistical significance for the tables are provided in Appendix F. All error bars represent one standard deviation.

Feature kernel operator. We define the *feature map* $\Phi : \mathcal{X} \rightarrow \mathbb{R}^p$ as the map from the input to the post-activations of the penultimate layer. For $1 \leq k \leq p$, denote the k^{th} *feature* as the k^{th} entry $\Phi_k(x)$ of $\Phi(x) = [\Phi_1(x), \dots, \Phi_p(x)]$. We define the *feature kernel operator* $\mathcal{T} : L^2(\mathcal{X}) \rightarrow L^2(\mathcal{X})$, generalization of self-correlation matrix in function space, as

$$\mathcal{T}[f](x') := \mathbf{E}_{x \sim q} \left[\sum_{k=1}^p \Phi_k(x) \Phi_k(x') f(x) \right], \quad \mathcal{T} = \sum_{k=1}^p |\Phi_k\rangle \langle \Phi_k|, \quad (1)$$

where $L^2(\mathcal{X})$ is the Hilbert space of square-integrable functions on \mathcal{X} (with distribution q). The second expression is \mathcal{T} in bra-ket notation. Using Mercer’s theorem [15], we can decompose the operator into eigenfunctions and eigenvalues

$$\mathcal{T} := \sum_{k=1}^p \rho_k |e_k\rangle \langle e_k|, \quad \mathcal{T}[e_k] = \rho_k e_k, \quad \langle e_k | e_l \rangle = \delta_{kl}, \quad (2)$$

where $\rho_k \in \mathbb{R}$ is a non-negative eigenvalue and $e_k : \mathcal{X} \rightarrow \mathbb{R}$ is the orthonormal eigenfunction. The operator \mathcal{T} and the eigenfunctions e_k play a key role in kernel regression with feature map Φ (i.e. $K(x, x') = \Phi(x)^T \Phi(x')$). The linear model (kernel) has inductive bias toward larger (eigenvalue) eigenfunctions [16–21] and generalizes better when larger eigenfunctions (larger ρ_k) also better describe the target function (larger $\langle e_k | f^* \rangle$) — also known as the task-model alignment [16]. See Appendix C for a gentle introduction.

Rich dynamics. Chizat et al. [2] introduced rich dynamics as deviations from the exponential saturation observed in linear models. Subsequent works [11, 22, 13] identified these dynamics as sigmoidal saturation or amplifying dynamics — arising from gradient descent in layerwise models — and connected them to phenomena like neural collapse [5], feature emergence [7], and grokking [11]. See Nam et al. [13] for a comprehensive overview.

Low-rank bias and neural collapse. Low-rank hidden representations naturally emerge in the rich regime, as shown by studies across linear networks [4, 23–27], unconstrained feature models [5, 28], and matrix factorization [29, 30]. These works find that gradient dynamics decouple into a minimal number of modes, governed by the rank of the input-output correlation matrix (often that of the output C), causing gradients to concentrate on those modes and produce low-rank representations. In practice, the low-rank bias is observed as neural collapse [6], which consists of four conditions NC1-4 stated in Appendix D. Although often associated with improved representations, neural collapse does not consistently imply better generalization [31–34], remaining largely a dynamical phenomenon [13]. See Kothapalli et al. [35] for an overview.

3 Richness measure and visualization method

We introduce a framework that consists of a dynamical richness measure and a visualization method. We will exploit the low-rank bias of rich dynamics to measure richness and show that it reduces to neural collapse as a special case. For visualization methods, we will generalize the natural metrics from kernel regression (linear models) to quantify the features’ cumulative quality Π^* , utilization $\hat{\Pi}$, and relative intensity ρ_k/ρ_1 (Eq. (5)), providing objective metrics for the evolution of features.

3.1 Low rank bias as richness measure

We define the *learned function space* $\hat{\mathcal{H}} = \text{span}\{\hat{f}_1, \dots, \hat{f}_C\}$ where $\hat{f}_k : \mathcal{X} \rightarrow \mathbb{R}$ is the k^{th} entry of the learned function (at any given time). In an ideal rich dynamics scenario, only the minimal number of features are learned throughout the dynamics and are sufficient to express (linearly span) the learned function space. Leveraging this idea, we define the minimal projection operator \mathcal{T}_{MP} .

Definition 1 (Minimum Projection (MP) operator). *For a neural network with learned function \hat{f} and features $\Phi(x)$, the corresponding \mathcal{T} is an MP-operator \mathcal{T}_{MP} if it can be expressed as*

$$\mathcal{T}_{MP}[u] = a_1 \langle \mathbf{1} | u \rangle \mathbf{1} + a_2 P_{\hat{\mathcal{H}}}(u) \quad \text{for all } u \in L^2(\mathcal{X}), \quad (3)$$

where $a_1, a_2 > 0$, $\mathbf{1}$ is a constant function, and $P_{\hat{\mathcal{H}}}$ is the orthogonal projection onto $\hat{\mathcal{H}}$.

Ignoring the constant function (setting $a_1 = 0$), whose discussion is deferred to Appendix D, the \mathcal{T}_{MP} is (up to a constant scale) a projection operator $P_{\hat{\mathcal{H}}}$ that removes all components orthogonal to $\hat{\mathcal{H}}$. If \mathcal{T} is \mathcal{T}_{MP} , the last-layer features span only a C -dimensional space that matches the learned function space, reflecting the low-rank structure characteristic of rich dynamics. We thus define the *low rank measure* \mathcal{D}_{LR} as the similarity between the \mathcal{T} — defined by the current features — and the MP-operator \mathcal{T}_{MP} — defined by the current learned function — as a metric for richness:

$$\mathcal{D}_{LR} := 1 - CKA(\mathcal{T}, \mathcal{T}_{MP}), \quad (4)$$

where CKA is the centered kernel alignment [36] with bounded value in $[0, 1]$. Because CKA is normalized and uses centered (zero-mean) alignment, the metric remains consistent for any a_1 and a_2 (Appendix B.3). We subtract the CKA measure from 1 so that lower values indicate richer dynamics, consistent with more widely used metrics of richness. The novelty of our metric \mathcal{D}_{LR} lies in using the minimum projection operator \mathcal{T}_{MP} .

Intuition. Our metric (Eq. (4)) estimates how many independent feature directions exist beyond those used to express the learned function. In rich dynamics, only the minimal necessary features are learned and used ($\mathcal{D}_{LR} = 0$); the earlier layers are sufficiently feature-learned to express the learned function. An excess of features suggests a bottleneck —such as limited expressivity in earlier layers— hindering feature learning of earlier layers.

Connection to neural collapse. Suppose that the empirical distribution coincides with the true distribution and the neural network perfectly classifies all labels with one-hot vectors. We show that if \mathcal{T} is an MP-operator, then the NC1 and NC2 conditions (Appendix D) of neural collapse hold. Let dagger \dagger denote pseudo inverse, A_i the set of datapoints with class label i , so the i^{th} learned function \hat{f}_i coincides with the one-hot indicator function for A_i . Following Papayan et al. [6], we define the i^{th} class mean vector as $\mu_i := \mathbb{E}_{x \in A_i}[\Phi(x)]$ and the global mean vector as $\bar{\mu} := C^{-1} \sum_{i=1}^C \mu_i$.

Proposition 1. *If \mathcal{T} is an MP-operator, then the NC1 condition (collapse of within-class variability) $\Sigma_b^\dagger \Sigma_W = 0$ holds, where inter-class covariance matrix Σ_b and intra-class covariance matrix Σ_W are*

$$\Sigma_b = \sum_{j=1}^C (\mu_j - \bar{\mu})(\mu_j - \bar{\mu})^T \quad \text{and} \quad \Sigma_W = \sum_{i=1}^C \mathbb{E}_{x \in A_i} [(\Phi(x) - \mu_i)(\Phi(x) - \mu_i)^T].$$

Proposition 2. *If \mathcal{T} is an MP-operator, then the NC2 condition (convergence of features to a simplex equiangular tight frame) holds:*

$$(\mu_i - \bar{\mu})^T (\mu_j - \bar{\mu}) \propto \delta_{ij} - \frac{1}{C}.$$

See Appendix D for proofs and further discussions.

Although the ideal criteria of \mathcal{T} is \mathcal{T}_{MP} implies neural collapse criteria as a special case, they differ in general: we measure how well **features (random variables or functions)** express the **learned function**, while neural collapse concerns how training **feature vectors** represent **class mean vectors**. Based on function space, our measure extends to test data, enables feature quality assessment (Eq. (5)), and is more robust (Fig. 2), extending beyond neural collapse (see Appendix D).

3.2 Visualization through decomposed features

So far, we have focused on a metric for dynamical richness. While metrics offer quantitative summaries, visualization by components reveals underlying structure and trends obscured by raw number — helping interpret whether an observed metric value is meaningfully small or large enough (e.g., Fig. 4). We also aim to incorporate feature improvement (thus quality) into these visualizations to encourage future work on its relationship with dynamical richness.

Bengio et al. [1] described feature learning as the process of learning better representations for a downstream model, such as the classifier. Building on this idea, we view the earlier layers, represented by the feature map $\Phi : \mathcal{X} \rightarrow \mathbb{R}^p$, as providing improved features for the final linear layer. Combined with our \mathcal{T} -dependent richness metric, this motivates a visualization method that extends the linear model analysis of \mathcal{T} (Appendix C).

Our framework quantifies three aspects (cumulative quality $\Pi^*(k)$, cumulative utilization $\hat{\Pi}(k)$, and relative eigenvalue ρ_k/ρ_1) of the last-layer features:

$$(i) : \Pi^*(k) = \sum_{j=1}^k \frac{\langle e_k | P_{\mathcal{H}^*} [e_k] \rangle^2}{\dim(\mathcal{H}^*)}, \quad (ii) : \hat{\Pi}(k) = \sum_{j=1}^k \frac{\langle e_k | P_{\hat{\mathcal{H}}} [e_k] \rangle^2}{\dim(\hat{\mathcal{H}})}, \quad (iii) : \rho_k/\rho_1, \quad (5)$$

where $\mathcal{H}^* = \text{span}\{f_1^*, \dots, f_C^*\}$ and $\hat{\mathcal{H}} = \text{span}\{\hat{f}_1, \dots, \hat{f}_C\}$ are the target and learned function spaces, and $P_{\mathcal{H}} : \mathcal{H} \rightarrow \mathcal{H}$ is the projection operator onto the space \mathcal{H} . All cumulative measures lie in $[0, 1]$, reflecting how well the top k features span the respective space. Notably, $\Pi^*(k)$ is analogous to the task-model alignment, quantifying the contribution of the top features in expressing the target.

These three measures together capture complementary views of feature learning. The cumulative quality ($\Pi^*(k)$) reflects how well the features align with the task (i.e., task-model alignment). The utilization ($\hat{\Pi}(k)$) indicates how many features are used by the final layer, while the relative eigenvalues (ρ_k/ρ_1) show their relative magnitudes or importance. The latter two ($\hat{\Pi}$ and ρ_k/ρ_1) decompose the deviation from $\mathcal{D}_{LR} = 0$ condition by visualizing how many features are used and how many are significant (non-negligible).

3.3 Approximating the metrics in practice

To calculate the eigenvalues and eigenfunctions (and thus the quality, utilization, and intensity) for a feature map Φ , we need the true input distribution q , which is, in principle, inaccessible. However, we can use Nyström method [37, 38] for a sufficiently large sample size of $n > p$ to approximate the eigenfunctions and eigenvalues of interest. We can create a $p \times p$ empirical self-covariance matrix Σ from n samples of $\Phi(x)$. By diagonalizing $\Sigma = U S U^T$, we can obtain the empirical eigenvectors and eigenvalues, which can be used to approximate the true eigenvalues and **eigenfunctions**:

$$\rho_k \approx s_k, \quad e_k(x) \approx \Phi(x)^T u_k / \sqrt{s_k}. \quad (6)$$

The algorithm is summarized in Algorithm 1.

Algorithm 1 Empirical eigenfunctions and eigenvalues

- 1: Φ, D_{tr} (Prepare a feature map Φ and D_{tr} : n samples of training set)
 - 2: $\phi \leftarrow \Phi(D_{tr})$ (forward transform the input samples to feature vectors)
 - 3: $U, S, U^T \leftarrow \text{SVD}(\phi\phi^T)$ (perform singular value decomposition)
 - 4: $[u_1, u_2, \dots, u_p] \leftarrow U$ (find the column vectors of U)
 - 5: **for** k in $1, 2, \dots, p$ **do**
 - 6: $\rho_k \leftarrow s_k$ (approximate eigenvalues)
 - 7: $e_k(x) \leftarrow \Phi(x)^T u_k / \sqrt{s_k}$ (approximate eigenfunctions)
 - 8: **end for**
-

Functions not vectors. Note that eigenfunctions $e_k' s$ are defined **beyond the training samples** used to compute ϕ and differ from the eigenvectors of the empirical self-covariance matrix. This enables us to evaluate feature quality — via inner products with the target function — on the **test set** rather than the training set, a capability not available for empirical eigenvectors.

Time complexity. The algorithm is computationally efficient in practice. The main cost in computing Eq. (6) is the SVD, typically with time complexity $\mathcal{O}(p^3)$. A good approximation requires only $n = \mathcal{O}(p)$ datapoints—more than the last layer width. Performing SVD on ϕ instead of $\phi\phi^T$ yields U and \sqrt{S} with $\mathcal{O}(p^3)$ cost. Because last layers are typically narrow (e.g., $p \approx 10^3$) and the algorithm requires just $n = \mathcal{O}(p)$ forward passes, the overall computation is lightweight.

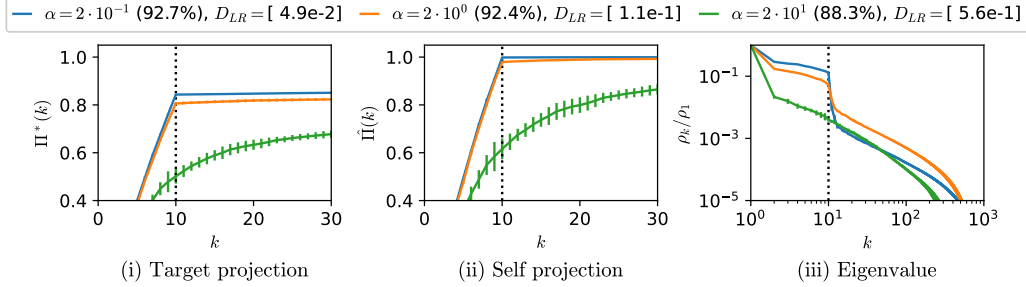
4 Comparison to prior measures of rich dynamics

Beyond performance — often used as a proxy for rich dynamics [2, 10] — three common metrics are: (1) similarity to the initial kernel, $\mathcal{S}_{init} = CKA(K_{init}, K_{learned}) \in [0, 1]$ [39], (2) the parameter norm $\|\theta\|_F^2$ [12], and (3) class separation from neural collapse, $NC1 = Tr(\Sigma_b^\dagger \Sigma_W)$ [6, 40–43], where Σ_b and Σ_W are the inter- and intra-class covariances (Proposition 1). Prior metrics have limitations as an independent measure of richness as they rely on the initial kernel, parameter norms, or class labels.

Epoch	0 (init)	200	α	$2 \cdot 10^{-1}$	$2 \cdot 10^0$	$2 \cdot 10^1$
Train Acc.↑	10.0%	10.2%	Train Acc.↑	100 %	100%	100%
Test Acc.↑	9.85%	10.0%	Test Acc.↑	92.7%	92.4%	88.3%
$\mathcal{D}_{LR} \downarrow$	0.59	1.0	$\mathcal{D}_{LR} \downarrow$	$4.9 \cdot 10^{-2}$	$1.1 \cdot 10^{-1}$	$5.6 \cdot 10^{-1}$
$\mathcal{S}_{init} \downarrow$	1.0	0.20	$\mathcal{S}_{init} \downarrow$	$6.8 \cdot 10^{-2}$	$4.1 \cdot 10^{-2}$	$5.2 \cdot 10^{-2}$
$\ \theta\ _F^2 \downarrow$	$3.1 \cdot 10^3$	$2.2 \cdot 10^{-5}$	$\ \theta\ _F^2 \downarrow$	$3.4 \cdot 10^3$	$3.2 \cdot 10^3$	$3.2 \cdot 10^3$
$NC1 \downarrow$	$1.2 \cdot 10^5$	$7.5 \cdot 10^{-14}$	$NC1 \downarrow$	$2.3 \cdot 10^4$	$3.2 \cdot 10^3$	$8.1 \cdot 10^2$

(a) Weight decay dynamics

(b) Target downscaling



(c) Visualization

Figure 2: **A 4-layer MLP trained on 10^3 MNIST samples.** (a) Training with larger weight decay 10^{-3} and smaller learning rate 10^{-6} . While our metric correctly indicates the lack of richness, all other metrics mistakenly suggest a significant rich dynamics with smaller post-training values. (b) Training with target downscaling α , where larger α leads to lazier dynamics. Only our measure correctly identifies the change in laziness. For a discussion on NC1, See Appendix F. (c) Our visualization methods for target downscaling, illustrating how lazier dynamics (ii) use more features and (iii) show a slower decay of eigenvalues (ignoring ρ_1 of constant function, see Appendix D).

Figure 2(a) shows an extreme case of training an MLP on MNIST with large weight decay and a negligible learning rate. Here, the dynamics are dominated by L2 weight decay, with little meaningful learning. While existing metrics often misinterpret this as rich behavior (smaller after training), our span-based measure correctly identifies the lack of dynamical richness (bigger after training). Figure 2(b,c) presents a more practical setting, where we tune laziness via target downscaling (i.e., $y \rightarrow y/\alpha$). Prior works [2, 3] show that scaling targets by a factor α induces lazier training where larger α implies greater laziness. A good metric should capture this. In Fig. 2(b), our measure **aligns with** α , while all other measures misalign with laziness. Finally, Fig. 2(c) visualizes the reduced dynamical richness by showing that more features are used and are significant as α increases.

Kernel distance from initialization (\mathcal{S}_{init}). Kernel deviation is a common measure of feature learning [2], often computed via the change in the neural tangent kernel (NTK) [3, 44, 45]. However, empirical NTK is computationally expensive in practice, so here we observe the change in the last-layer feature kernel instead. Importantly, kernel deviation can be misleading in deep, rich-training

regimes where most practical training occurs. While it detects movement away from the initial kernel, it cannot distinguish different degrees of richness once the dynamics are non-lazy, nor does it capture the specific low-rank biases characteristic of rich feature learning.

Parameter norm ($\|\theta\|_F^2$). The parameter norm, used in Lyu et al. [12] as a proxy for richness, may offer a limited perspective as it ignores the learning dynamics and is unbounded in scale. Indeed, networks can enter a rich regime even as their weight norm increases [22, 46]. While smaller norms do often correlate with rich dynamics in practice, this is because small weights tend to promote rich dynamics [10, 47, 13, 4, 48] — not because rich dynamics inherently produce small norms. In fact, rich dynamics depend on broader factors such as network layer imbalance [46, 22, 11, 13].

Neural collapse measure ($NC1$). Separation-based metrics measure how training samples deviate relative to class boundaries [6, 40–43]. They are designed for the terminal phase of training and depend heavily on class labels (thus training accuracy) and especially the output scale — making them unreliable during training. Their unbounded nature further complicates interpretation. As shown in Fig. 2(a), they are overly sensitive to output scaling, falsely suggesting increased richness under weight decay.

Our measure (\mathcal{D}_{LR}). Our proposed metric evaluates the alignment between features and the learned function, achieving its optimum when they span the same space isotropically (i.e., a scaled projection operator). Our metric exploits the low-rank bias of greedy dynamics through the alignment and is normalized between $[0, 1]$. Crucially, it does so without relying on class labels, accuracy, or the initial kernel, making the measure more appealing as an independent measure of richness.

5 Observations from our visualization methods

In this section, we present a series of empirical findings to demonstrate the effectiveness of our visualization framework (Eq. (5)) and to highlight observations that open revenues for future theoretical studies. We revisit several known phenomena by our visualization framework, such as the emergence of rich dynamics in the absence of underlying data structure (Fig. 3) and the transition from lazy to rich regime during grokking (Fig. 4). We also report novel observations, including the role of training sample size (Fig. 5) and batch normalization (Fig. 6) in encouraging richness, and a correlation between the quality and intensity of rich dynamics during training (Fig. 7).

For completeness, additional empirical results are provided in Appendices D and E, including evidence of low-rank bias without weight decay (Fig. 14), the impact of the learning rate on dynamical richness (Fig. 15), the richer-to-lazier transition on MLP (Fig. 16), and the dependence of low-rank bias on the dimensionality of the output function rather than the number of target classes (Fig. 12).

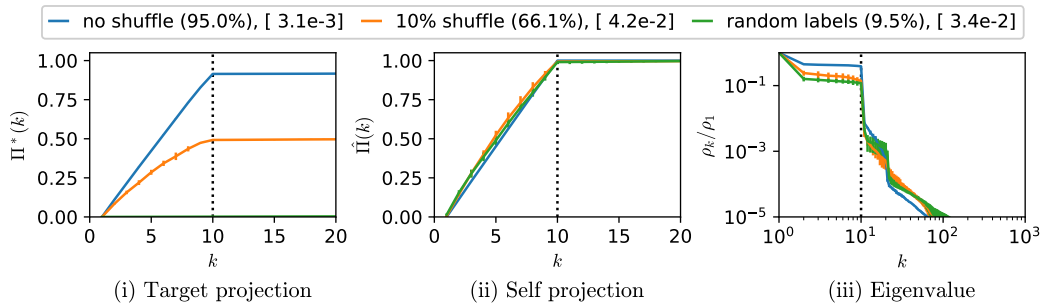


Figure 3: **ResNet18 on 10^4 CIFAR-10 datapoints with shuffled labels.** Models are trained with 0% (blue), 10% (orange), and 100% (green) label shuffling. As shown in the square brackets, all exhibit rich dynamics with $\mathcal{D}_{LR} < 0.1$. Visualizations in (ii) and (iii) confirm the use of the top 10 significant features, but varying feature qualities (i) lead to varying test accuracies, shown in parentheses.

Rich dynamics without underlying data structure. Fig. 3 illustrates that rich dynamics can occur independently of representation enhancement or underlying data structure. We trained ResNet18 on

CIFAR-10 with varying levels of label shuffling and observed that even with fully randomized labels, the model enters the rich regime. This suggests that the dynamical low-rank bias is strong enough to collapse expressive networks into minimal representations, consistent with prior observations of neural collapse under random labeling [31, 33].

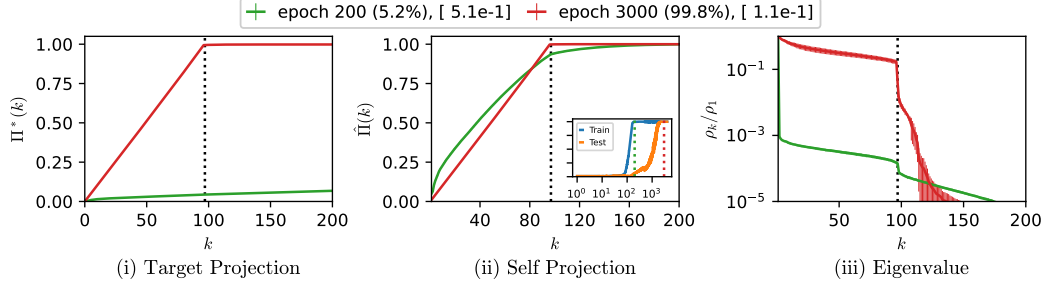


Figure 4: **Grokking as a transition from the lazy to rich regime.** A 2-layer transformer is trained on the modular p division task. The inset in the middle shows the training and test accuracies, where green and red vertical lines indicate before and after grokking (steps 200 and 3000). Our metric in square brackets shows the transition into the rich regime, while our visualization shows a clear difference in the use of features.

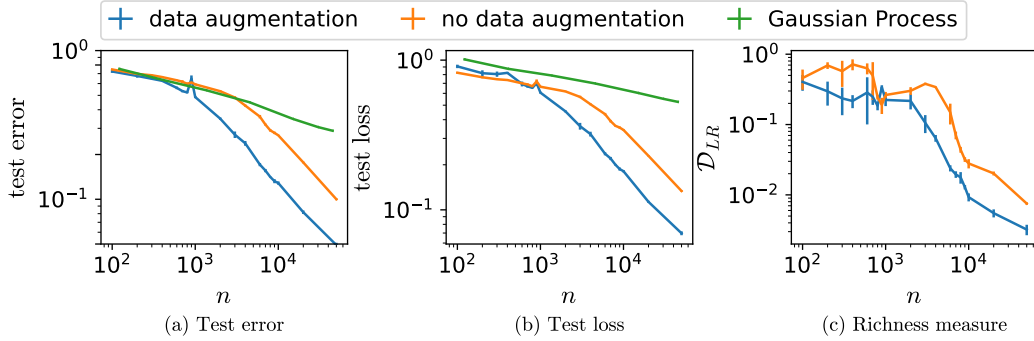


Figure 5: **Learning curve and feature learning metric.** (a): Learning curves of ResNet18 on CIFAR10. Both error (a) and loss (b) learning curves show a transition to a faster-decaying power law with additional data near $n \approx 10^3$. This correlates with the shift in decay of the richness measure \mathcal{D}_{LR} in (c), suggesting a transition into richer dynamics. A linear model (Gaussian process) was plotted in (a,b) to highlight the transition into faster-decaying learning curve.

Grokking. Fig. 4 confirms that grokking involves a transition from a lazy, overfitting regime to a rich, generalizing one [10–13]. While prior work has analyzed the dynamics, the transition into the rich regime was often inferred from the grokking behavior of the performance. Our metric provides an independent measure that aligns and supports previous studies.

Learning curves. In Fig. 5, the learning curve follows a power law but exhibits a shift in the exponent at a dataset size n , which coincides with a sudden transition into the rich regime. This suggests that a sufficiently large number of data points is critical for initiating rich dynamics — a promising observation toward better understanding feature learning dynamics.

Batch normalization. Fig. 6 shows a novel observation that VGG16 without batch norm is in the lazy regime, while adding batch norm leads to the rich regime. While the performance benefits of batch norm are well known, our method offers a new perspective on its influence over lazy vs. rich dynamics, shedding light on *why* it improves performance.

Rich feature learning. Fig. 7 reveals another novel pattern in feature learning dynamics: feature quality correlates with feature intensity during training, with larger features improving faster. While

it is expected that a generalizing model in the rich regime obtains a few high-quality features after training, the correlation between quality and intensity *during* training has not been previously observed or studied. Interestingly, it appears to contrast with the silent alignment [49], which suggests quality (dynamically) precedes intensity — highlighting a new direction for future research.

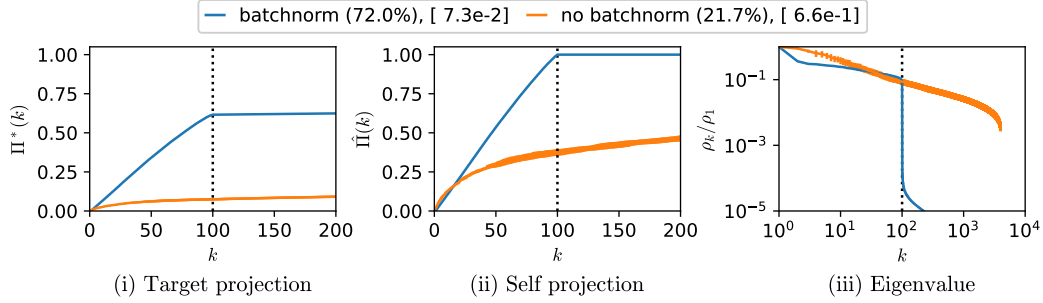


Figure 6: **VGG16 on CIFAR-100 with and without batch normalization.** Adding batch normalization results in not only a significant performance boost, but shifts the model from the lazy to rich regime (\mathcal{D}_{LR} drops from 0.66 to 0.07). The visualization highlights this shift, showing that only a minimal number (100) of features are actively used when batch normalization is present.

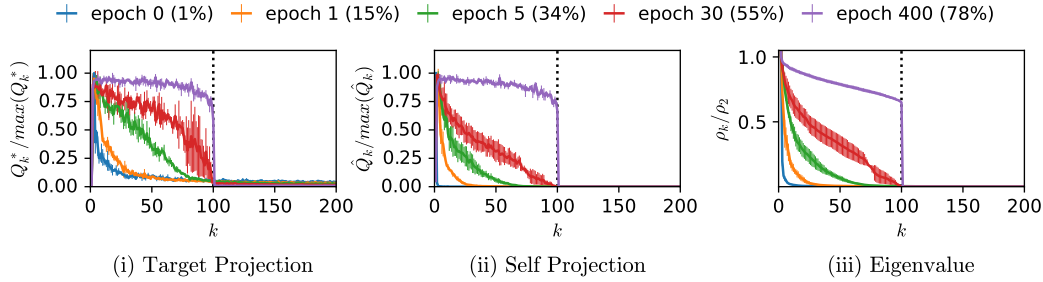


Figure 7: **Correlation among dynamics of feature quality, utilization, and intensity.** We show individual metrics (e.g., $Q^*(k) := \Pi^*(k) - \Pi^*(k-1)$) instead of cumulative metrics ($\Pi^*(k)$ and $\hat{\Pi}(k)$) at different epochs for ResNet18 on CIFAR-100, normalized for better presentation. Larger intensity features exhibit higher quality and utilization during training.

6 Discussion and Conclusion

In this paper, we introduced a principled framework for measuring dynamical richness independently of representation improvement. Our low-rank-based metric \mathcal{D}_{LR} , along with a complementary function-space visualization, provides tools to analyze training dynamics and feature improvement separately within a unified framework.

Our metric builds on the low-rank bias in rich regimes and reduces to neural collapse under mild assumptions (Propositions 1 and 2), offering generalization of prior studies. Unlike prior proxies — e.g., parameter norms or neural collapse metrics — \mathcal{D}_{LR} operates directly in function space, assessing how efficiently the model expresses its learned function using minimal number of features.

Empirically, our richness metric decouples performance from dynamics (Figs. 1 and 3), captures lazy-to-rich transitions (Figs. 2 and 4), and detects richness where prior measures fail (Fig. 2). Our visualizations highlight these differences more directly, revealing novel patterns (Figs. 5 to 7) that invite further theoretical study of feature learning.

Limitations. The current form of \mathcal{T}_{MP} is limited to orthogonal and isotropic target functions. While this covers most classification tasks, a more general setup would be preferable. Additionally, our framework provides a lightweight metric but focuses only on last-layer features, leaving the dynamics of the entire network dynamics unexplored.

Conclusion. Our metric and visualizations offer a concrete step toward understanding feature learning from both representational and dynamical perspectives. We believe these tools can help bridge empirical findings with theoretical insights and inspire new discoveries through the details they reveal. In future work, we will address current limited scope of balanced tasks.

Acknowledgment

We thank Charles London, Zohar Ringel, and Shuofeng Zhang for their helpful comments. NF acknowledges the UKRI support through the Horizon Europe guarantee Marie Skłodowska-Curie grant (EP/X036820/1). SL was supported by the National Research Foundation of Korea (NRF) grants No.2020R1A5A1016126 and No.RS-2024-00462910. The authors would also acknowledge support from His Majesty’s Government in the development of this research. CM acknowledges funding from an EPSRC iCASE grant with IBM (grant number EP/S513842/1). SH gratefully acknowledge partial support from NSF grants DMS-2209975, 2015341, 20241842, NSF grant 2023505 on Collaborative Research: Foundations of Data Science Institute (FODSI), the NSF and the Simons Foundation for the Collaboration on the Theoretical Foundations of Deep Learning through awards DMS-2031883 and 814639, and NSF grant MC2378 to the Institute for Artificial CyberThreat Intelligence and OperationN (ACTION). The authors would also acknowledge support from His Majesty’s Government in the development of this research.

References

- [1] Yoshua Bengio, Aaron Courville, and Pascal Vincent. Representation learning: A review and new perspectives. *IEEE transactions on pattern analysis and machine intelligence*, 35(8):1798–1828, 2013.
- [2] Lenaic Chizat, Edouard Oyallon, and Francis Bach. On lazy training in differentiable programming. *Advances in neural information processing systems*, 32, 2019.
- [3] Mario Geiger, Stefano Spigler, Arthur Jacot, and Matthieu Wyart. Disentangling feature and lazy training in deep neural networks. *Journal of Statistical Mechanics: Theory and Experiment*, 2020(11):113301, 2020.
- [4] Andrew M. Saxe, James L. McClelland, and Surya Ganguli. Exact solutions to the nonlinear dynamics of learning in deep linear neural networks. In Yoshua Bengio and Yann LeCun, editors, *2nd International Conference on Learning Representations, ICLR 2014, Banff, AB, Canada, April 14-16, 2014, Conference Track Proceedings*, 2014.
- [5] Dustin G Mixon, Hans Parshall, and Jianzong Pi. Neural collapse with unconstrained features. *arXiv preprint arXiv:2011.11619*, 2020.
- [6] Vardan Papyan, XY Han, and David L Donoho. Prevalence of neural collapse during the terminal phase of deep learning training. *Proceedings of the National Academy of Sciences*, 117(40):24652–24663, 2020.
- [7] Yoonsoo Nam, Nayara Fonseca, Seok Hyeong Lee, Chris Mingard, and Ard A. Louis. An exactly solvable model for emergence and scaling laws in the multitask sparse parity problem. In *The Thirty-eighth Annual Conference on Neural Information Processing Systems*, 2024.
- [8] Tom Brown, Benjamin Mann, Nick Ryder, Melanie Subbiah, Jared D Kaplan, Prafulla Dhariwal, Arvind Neelakantan, Pranav Shyam, Girish Sastry, Amanda Askell, et al. Language models are few-shot learners. *Advances in neural information processing systems*, 33:1877–1901, 2020.
- [9] Jared Kaplan, Sam McCandlish, Tom Henighan, Tom B Brown, Benjamin Chess, Rewon Child, Scott Gray, Alec Radford, Jeffrey Wu, and Dario Amodei. Scaling laws for neural language models. *arXiv preprint:2001.08361*, 2020.
- [10] Tanishq Kumar, Blake Bordelon, Samuel J. Gershman, and Cengiz Pehlevan. Grokking as the transition from lazy to rich training dynamics. In *The Twelfth International Conference on Learning Representations*, 2024.

- [11] Daniel Kunin, Allan Raventos, Clémentine Carla Juliette Dominé, Feng Chen, David Klindt, Andrew M Saxe, and Surya Ganguli. Get rich quick: exact solutions reveal how unbalanced initializations promote rapid feature learning. In *The Thirty-eighth Annual Conference on Neural Information Processing Systems*, 2024.
- [12] Kaifeng Lyu, Jikai Jin, Zhiyuan Li, Simon Shaolei Du, Jason D. Lee, and Wei Hu. Dichotomy of early and late phase implicit biases can provably induce grokking. In *The Twelfth International Conference on Learning Representations*, 2024.
- [13] Yoonsoo Nam, Seok Hyeong Lee, Clementine Domine, Yea Chan Park, Charles London, Wonyl Choi, Niclas Goring, and Seungjai Lee. Position: Solve layerwise linear models first to understand neural dynamical phenomena (neural collapse, emergence, lazy/rich regime, and grokking). *arXiv preprint arXiv:2502.21009*, 2025.
- [14] Alethea Power, Yuri Burda, Harri Edwards, Igor Babuschkin, and Vedant Misra. Grokking: Generalization beyond overfitting on small algorithmic datasets. *arXiv:2201.02177*, 2022.
- [15] James Mercer. Xvi. functions of positive and negative type, and their connection the theory of integral equations. *Philosophical transactions of the royal society of London. Series A, containing papers of a mathematical or physical character*, 209(441-458):415–446, 1909.
- [16] Blake Bordelon, Abdulkadir Canatar, and Cengiz Pehlevan. Spectrum dependent learning curves in kernel regression and wide neural networks. In *International Conference on Machine Learning*, pages 1024–1034. PMLR, 2020.
- [17] Arthur Jacot, Berfin Simsek, Francesco Spadaro, Clément Hongler, and Franck Gabriel. Kernel alignment risk estimator: Risk prediction from training data. *Advances in Neural Information Processing Systems*, 33:15568–15578, 2020.
- [18] Stefano Spigler, Mario Geiger, and Matthieu Wyart. Asymptotic learning curves of kernel methods: empirical data versus teacher–student paradigm. *Journal of Statistical Mechanics: Theory and Experiment*, 2020(12):124001, 2020.
- [19] Abdulkadir Canatar, Blake Bordelon, and Cengiz Pehlevan. Spectral bias and task-model alignment explain generalization in kernel regression and infinitely wide neural networks. *Nature communications*, 12(1):2914, 2021.
- [20] Hugo Cui, Bruno Loureiro, Florent Krzakala, and Lenka Zdeborová. Generalization error rates in kernel regression: The crossover from the noiseless to noisy regime. *Advances in Neural Information Processing Systems*, 34:10131–10143, 2021.
- [21] Ouns El Harzli, Bernardo Cuenca Grau, Guillermo Valle-Pérez, and Ard A Louis. Double-descent curves in neural networks: a new perspective using gaussian processes. In *Proceedings of the AAAI Conference on Artificial Intelligence*, volume 38, pages 11856–11864, 2024.
- [22] Clémentine Carla Juliette Dominé, Nicolas Anguita, Alexandra Maria Proca, Lukas Braun, Daniel Kunin, Pedro A. M. Mediano, and Andrew M Saxe. From lazy to rich: Exact learning dynamics in deep linear networks. In *The Thirteenth International Conference on Learning Representations*, 2025.
- [23] Ziwei Ji and Matus Telgarsky. Gradient descent aligns the layers of deep linear networks. In *International Conference on Learning Representations*, 2019.
- [24] Sanjeev Arora, Nadav Cohen, Noah Golowich, and Wei Hu. A convergence analysis of gradient descent for deep linear neural networks. In *7th International Conference on Learning Representations*, 2019.
- [25] Andrew K. Lampinen and Surya Ganguli. An analytic theory of generalization dynamics and transfer learning in deep linear networks. In *7th International Conference on Learning Representations*, 2019.
- [26] Gauthier Gidel, Francis Bach, and Simon Lacoste-Julien. Implicit regularization of discrete gradient dynamics in linear neural networks. *Advances in Neural Information Processing Systems*, 32, 2019.

- [27] Salma Tarmoun, Guilherme Franca, Benjamin D Haeffele, and Rene Vidal. Understanding the dynamics of gradient flow in overparameterized linear models. In *International Conference on Machine Learning*, pages 10153–10161. PMLR, 2021.
- [28] Cong Fang, Hangfeng He, Qi Long, and Weijie J Su. Layer-peeled model: Toward understanding well-trained deep neural networks. *arXiv preprint arXiv:2101.12699*, 4, 2021.
- [29] Sanjeev Arora, Nadav Cohen, Wei Hu, and Yuping Luo. Implicit regularization in deep matrix factorization. *Advances in Neural Information Processing Systems*, 32, 2019.
- [30] Zhiyuan Li, Yuping Luo, and Kaifeng Lyu. Towards resolving the implicit bias of gradient descent for matrix factorization: Greedy low-rank learning. *arXiv preprint arXiv:2012.09839*, 2020.
- [31] Zhihui Zhu, Tianyu Ding, Jinxin Zhou, Xiao Li, Chong You, Jeremias Sulam, and Qing Qu. A geometric analysis of neural collapse with unconstrained features. *Advances in Neural Information Processing Systems*, 34:29820–29834, 2021.
- [32] Duc Anh Nguyen, Ron Levie, Julian Lienen, Gitta Kutyniok, and Eyke Hüllermeier. Memorization-dilation: Modeling neural collapse under label noise. *arXiv preprint arXiv:2206.05530*, 2022.
- [33] Like Hui, Mikhail Belkin, and Preetum Nakkiran. Limitations of neural collapse for understanding generalization in deep learning. *arXiv preprint arXiv:2202.08384*, 2022.
- [34] Jingtong Su, Ya Shi Zhang, Nikolaos Tsilivis, and Julia Kempe. On the robustness of neural collapse and the neural collapse of robustness. *arXiv preprint arXiv:2311.07444*, 2023.
- [35] Vignesh Kothapalli, Ebrahim Rasromani, and Vasudev Awatramani. Neural collapse: A review on modelling principles and generalization. *arXiv preprint arXiv:2206.04041*, 2022.
- [36] Simon Kornblith, Mohammad Norouzi, Honglak Lee, and Geoffrey Hinton. Similarity of neural network representations revisited. In *International conference on machine learning*, pages 3519–3529. PMLR, 2019.
- [37] Christopher TH Baker and RL Taylor. The numerical treatment of integral equations. *Journal of Applied Mechanics*, 46(4):969, 1979.
- [38] Christopher KI Williams and Carl Edward Rasmussen. *Gaussian processes for machine learning*, volume 2. MIT press Cambridge, MA, 2006.
- [39] Greg Yang and Edward J Hu. Tensor programs iv: Feature learning in infinite-width neural networks. In *International Conference on Machine Learning*, pages 11727–11737. PMLR, 2021.
- [40] James Stevens et al. *Applied multivariate statistics for the social sciences*, volume 4. Lawrence erlbaum associates Mahwah, NJ, 2002.
- [41] Hangfeng He and Weijie J Su. A law of data separation in deep learning. *Proceedings of the National Academy of Sciences*, 120(36):e2221704120, 2023.
- [42] Jing Xu and Haoxiong Liu. Quantifying the variability collapse of neural networks. In *International Conference on Machine Learning*, pages 38535–38550. PMLR, 2023.
- [43] Peter Súkeník, Marco Mondelli, and Christoph Lampert. Neural collapse versus low-rank bias: Is deep neural collapse really optimal? *arXiv preprint arXiv:2405.14468*, 2024.
- [44] Arthur Jacot, Franck Gabriel, and Clément Hongler. Neural tangent kernel: Convergence and generalization in neural networks. In *Advances in neural information processing systems*, pages 8571–8580, 2018.
- [45] Greg Yang and Edward J. Hu. Tensor programs IV: Feature learning in infinite-width neural networks. In *Proceedings of the 38th International Conference on Machine Learning*, pages 11727–11737. PMLR. ISSN: 2640-3498.

- [46] Lukas Braun, Clémentine Dominé, James Fitzgerald, and Andrew Saxe. Exact learning dynamics of deep linear networks with prior knowledge. *Advances in Neural Information Processing Systems*, 35:6615–6629, 2022.
- [47] Alexander Atanasov, Alexandru Meterez, James B Simon, and Cengiz Pehlevan. The optimization landscape of sgd across the feature learning strength. *arXiv preprint arXiv:2410.04642*, 2024.
- [48] Andrew M Saxe, James L McClelland, and Surya Ganguli. A mathematical theory of semantic development in deep neural networks. *Proceedings of the National Academy of Sciences*, 116(23):11537–11546, 2019.
- [49] Alexander Atanasov, Blake Bordelon, and Cengiz Pehlevan. Neural networks as kernel learners: The silent alignment effect. *arXiv preprint arXiv:2111.00034*, 2021.
- [50] Aristide Baratin, Thomas George, César Laurent, R Devon Hjelm, Guillaume Lajoie, Pascal Vincent, and Simon Lacoste-Julien. Implicit regularization via neural feature alignment. In *International Conference on Artificial Intelligence and Statistics*, pages 2269–2277. PMLR, 2021.
- [51] Yizhang Lou, Chris E Mingard, and Soufiane Hayou. Feature learning and signal propagation in deep neural networks. In *International Conference on Machine Learning*, pages 14248–14282. PMLR, 2022.
- [52] Mark O Hill. Diversity and evenness: a unifying notation and its consequences. *Ecology*, 54(2):427–432, 1973.
- [53] Hervé Abdi and Lynne J Williams. Principal component analysis. *Wiley interdisciplinary reviews: computational statistics*, 2(4):433–459, 2010.
- [54] James B Simon, Madeline Dickens, Dhruva Karkada, and Michael R DeWeese. The eigenlearning framework: A conservation law perspective on kernel regression and wide neural networks. *Transactions on Machine Learning Research*, 2023.
- [55] Andrew Saxe, Shagun Sodhani, and Sam Jay Lewallen. The neural race reduction: Dynamics of abstraction in gated networks. In *International Conference on Machine Learning*, pages 19287–19309. PMLR, 2022.
- [56] Li Deng. The mnist database of handwritten digit images for machine learning research. *IEEE Signal Processing Magazine*, 29(6):141–142, 2012.
- [57] Alex Krizhevsky, Vinod Nair, and Geoffrey Hinton. Cifar-10 (canadian institute for advanced research).
- [58] Adam Paszke, Sam Gross, Francisco Massa, Adam Lerer, James Bradbury, Gregory Chanan, Trevor Killeen, Zeming Lin, Natalia Gimelshein, Luca Antiga, Alban Desmaison, Andreas Kopf, Edward Yang, Zachary DeVito, Martin Raison, Alykhan Tejani, Sasank Chilamkurthy, Benoit Steiner, Lu Fang, Junjie Bai, and Soumith Chintala. Pytorch: An imperative style, high-performance deep learning library. In *Advances in Neural Information Processing Systems* 32, pages 8024–8035. Curran Associates, Inc., 2019.
- [59] Preetum Nakkiran, Gal Kaplun, Yamini Bansal, Tristan Yang, Boaz Barak, and Ilya Sutskever. Deep double descent: Where bigger models and more data hurt. *Journal of Statistical Mechanics: Theory and Experiment*, 2021(12):124003, 2021.

A Glossary

Symbol.	Name	Definition	Ref
C	Class count	The number of classes.	Section 2
p	Layer width	The width of the last layer	Section 2
n	Sample count	The number of training samples	Section 2
\mathcal{X}	Input space	Space of inputs	Section 2
q	Input distribution	The probability distribution that generates samples in the input space.	Section 2
Φ	Feature map	A map from input to post-activation of the penultimate layer (the activations fed to the last layer).	Section 2
$\Phi(x)$	(Last layer) Features	A p -dimensional random variable or the post-activation of penultimate layer for $x \sim q$.	Section 2
\mathcal{T}	(Feature kernel) integral operator	A map from Hilbert space to Hilbert space that depends on $\Phi(x)$, $x \sim q$ (typically the last layer features)	Eq. (1)
\mathcal{T}_{MP}	Minimum projection operator	A special set of operators that depends on the learned function \hat{f} .	Definition 1
e_k	k^{th} eigenfunction	The eigenfunction of \mathcal{T} .	Eq. (2)
ρ_k	k^{th} eigenvalue	The eigenvalue of \mathcal{T} .	Eq. (2)
\hat{f}	Learned function	A C -dimensional vector output function $\hat{f} : \mathcal{X} \rightarrow \mathbb{R}^C$ expressed by the neural network.	Section 2
f^*	Target function	A C -dimensional vector output function $f^* : \mathcal{X} \rightarrow \mathbb{R}^C$ with correct labels. The output is always a one-hot vector (up to a scaling constant).	Section 2
\mathcal{H}^*	Target function space	Space linearly spanned by the entries of the target function.	Section 3
$\hat{\mathcal{H}}$	Learned function space	Space linearly spanned by the entries of the learned function	Section 3
$P_{\mathcal{H}}$	Projection operator	Projection operator onto \mathcal{H} . If $\mathcal{H} = \text{span}\{e_1, e_2, \dots, e_p\}$, where e_k 's are orthonormal, the the projection operator is given as $P_{\mathcal{H}} = \sum_{k=1}^p e_k\rangle \langle e_k $.	Section 3
α	Downscale constant	Prefactor that downscaling the target such that $y \rightarrow y/\alpha$	Section 4
Σ_b	Inter-class covariance matrix	Covariance of class mean vectors for the training set.	Eq. (34)
Σ_W	Intra-class covariance matrix	Covariance of training feature vectors within given class.	Eq. (33)
$CKA(\cdot, \cdot)$	Centered kernel alignment	Alignment measure between two matrices or operators. It is normalized between $[0, 1]$ and ignores the mean (for matrices) or constant function (for operators)	Eq. (7)
$\ \theta\ _F^2$	Parameter norm	Norm of all parameters in the model. It was used as richness measure with smaller value meaning richer dynamics.	Section 4
\mathcal{D}_{LR}	low rank metric	Our proposed metric of dynamical richness. Smaller is richer.	Eq. (4)
\mathcal{S}_{init}	Kernel deviation	The CKA measure between the learned and initial kernel.	Section 4
$NC1$	Neural collapse metric	The trace of $\Sigma_b^\dagger \Sigma_W$, measuring the training feature vectors variance compared to class boundaries.	Proposition 1
$\Pi^*(k)$	Cumulative quality	Measure of how well the first k eigenfunctions span the target function space.	Eq. (5)
$\hat{\Pi}(k)$	Cumulative utilization	Measure of how well the first k eigenfunctions span the learned function space.	Eq. (5)
$Q^*(k)$	Quality	Per-feature quality or $\Pi^*(k) - \Pi^*(k-1)$ where $\Pi^*(0) = 0$	Fig. 7
$\hat{Q}(k)$	Utilization	Per-feature utilization or $\hat{\Pi}(k) - \hat{\Pi}(k-1)$ where $\hat{\Pi}(0) = 0$	Fig. 7

B Technical supplementary material

Here, we introduce technical terms used in the main text and the following appendices.

B.1 Bra-ket notation

In physics, bra-ket notations are widely used to express the inner product in function space. In our paper, we use them to avoid overload of expectations and to clarify that we are using functions. Note that we use bra-ket notation for the expectation over the true input distribution only:

$$\langle f|g \rangle = \mathbf{E}_{x \sim q}[f(x)g(x)].$$

The notation is also useful for expressing operators such as \mathcal{T} :

$$\mathcal{T}[f](x) = \sum_{k=1}^p |\Phi_k\rangle \langle \Phi_k|f\rangle = [\Phi_1 \langle \Phi_1|f\rangle, \dots, \Phi_p \langle \Phi_p|f\rangle].$$

Because \mathcal{T} maps vector function $f : \mathcal{X} \rightarrow \mathbb{R}^p$ to a vector function, $\mathcal{T}[f] : \mathcal{X} \rightarrow \mathbb{R}^p$ is also a vector function with

$$\mathcal{T}[f](x) = [\Phi_1(x) \langle \Phi_1|f\rangle, \dots, \Phi_p(x) \langle \Phi_p|f\rangle],$$

where $\langle \Phi_k|f\rangle$ are scalars and $\Phi_k : \mathcal{X} \rightarrow \mathbb{R}$ are functions.

B.2 Features are random variables and (well-behaved) random variables form a Hilbert space

In machine learning, textbooks often overlook the mathematical distinction between feature maps and features, treating them as interchangeable. However, they are fundamentally different.

A feature map is a function $f : \mathcal{X} \rightarrow \mathcal{Y}$, defined independently of any distribution. A feature, by contrast, is a random variable induced by applying a feature map to inputs drawn from a distribution q over \mathcal{X} .

Features are therefore distribution-dependent: applying the same feature map to different input distributions yields different features. For instance, a fixed neural network defines a feature map, but the resulting features — such as last-layer activations — will differ between MNIST and Fashion-MNIST due to changes in the input distribution. The distinction also applies to kernel operators $\mathcal{T} : \mathcal{H} \rightarrow \mathcal{H}$ (distribution dependent) and kernels $K : \mathcal{X} \times \mathcal{X} \rightarrow \mathbb{R}$ (distribution independent).

The distinction becomes more important when we wish to discuss Hilbert space. A Hilbert space requires an inner product between functions (feature maps), which depends on the underlying distribution. For example, $\sin(x)$ and $\sin(2x)$ are orthogonal for $q = \text{unif}[0, 2\pi]$ where $\int_0^{2\pi} \sin(x) \sin(2x) dx = 0$, but not for unit Gaussian distribution $q = \mathcal{N}(0, 1)$ where $\int_{-\infty}^{\infty} \sin(x) \sin(2x) e^{-x^2/2} dx \neq 0$.

For an underlying probability distribution and a set of functions (feature maps), we can form a Hilbert space. A common example of a Hilbert space will be the set of solutions expressed by a linear model such as

$$f(x) = w_1 x + w_2 x^2 + w_3 x^3.$$

Assuming the features $[x, x^2, x^3]$ are linearly independent on input distribution q , they form a 3-dimensional Hilbert space.

B.3 Centered kernel alignment

The centered kernel alignment (CKA) [36] measures the similarity between two matrices or operators, and are commonly used for tracking the evolution of NTK [50, 51]:

$$CKA(A, B) = \frac{\text{Tr}(c(A)c(B))}{\|c(A)\|_F \|c(B)\|_F}, \quad (7)$$

where $c(A) = (I - |\mathbf{1}\rangle \langle \mathbf{1}|)A(I - |\mathbf{1}\rangle \langle \mathbf{1}|)$ is centering operator, where I is identity, $|\mathbf{1}\rangle$ is the constant function or constant vector, and $\|\cdot\|_F$ is Frobenius norm. The centering operator removes the constant

shift. The analogy is measuring the similarity of two multivariate Gaussian random variables by comparing their covariance matrices $\mathbf{E}[(X - \mathbf{E}[X])(X - \mathbf{E}[X])^T]$ instead of their autocorrelation matrices $\mathbf{E}[XX^T]$.

For \mathcal{T}_{MP} , if the learned function space $\hat{\mathcal{H}}$ contains the constant function — which is empirically true throughout the training for all our experiments and always true if it perfectly fits the training samples (Appendix D) — $c(\mathcal{T}_{MP})/\|c(\mathcal{T}_{MP})\|_F$ becomes an orthogonal projection operator on the constant complement of $\hat{\mathcal{H}}$, and is independent of the values of a_1 and a_2 .

B.4 Effective dimension

A covariance matrix or an integral operator may be fully ranked, but their eigenvalues may decay fast (e.g., by a power-law). The small eigendirections are often negligible, and researchers use various effective dimensions to measure the number of **significant** dimensions. In this appendix, we will use the exponent of entropy [52] to measure the effective dimension.

For a matrix or an operator with positive eigenvalues $[\rho_1, \dots, \rho_p]$, the effective dimension is

$$\exp \left(- \sum_{i=1}^p \frac{\rho_i}{\sum_{j=1}^p \rho_j} \ln \left(\frac{\rho_i}{\sum_{j=1}^p \rho_j} \right) \right). \quad (8)$$

Note that the effective dimension, the exponential of Shannon entropy, is d when the eigenvalues have d equal non-zero entries. A slower decay of entries of ρ (in non-increasing order of entries) generally yields a higher effective dimension than a vector with a faster decay.

The effective dimension of a matrix (operator) can be interpreted as the number of linearly independent vectors (functions) needed to effectively describe the matrix (operator). This is similar in spirit to the principal component analysis (PCA) [53] in that only the directions with significant variance are considered.

As discussed in Appendix D, the first eigenfunction is always a constant function, which is irrelevant for our measure \mathcal{D}_{LR} and dynamical interpretation. Because the first eigenvalue is often much larger than other significant eigenvalues, we use

$$D_{eff}(\rho) := 1 + \exp \left(- \sum_{i=2}^p \frac{\rho_i}{\sum_{j=2}^p \rho_j} \ln \left(\frac{\rho_i}{\sum_{j=2}^p \rho_j} \right) \right). \quad (9)$$

C Linear models, features, and their inductive bias

Here, we will introduce the recent findings on the inductive bias of linear models and demonstrate the significance of eigenvalues and eigenfunctions of \mathcal{T} . Linear regression or kernel regression is a rare case where its inductive bias is analytically calculable [16–21, 54]. For a given feature map $\Phi : \mathcal{X} \rightarrow \mathbb{R}^p$ or kernel $K(x, x') = \Phi(x)^T \Phi(x')$, the model is expressed as the p dimensional (p can be infinite) linear model

$$\hat{f}(x; w) = \sum_{k=1}^p w_k \Phi_k(x). \quad (10)$$

The objective of (ridgeless) regression is to minimize the following empirical loss

$$\mathcal{L}_{emp}(\hat{f}) = \frac{1}{2} \sum_{i=1}^n \left| \hat{f}(x^{(i)}) - f^*(x^{(i)}) \right|^2 + \lim_{\lambda \rightarrow 0} \lambda \|w\|_F^2, \quad (11)$$

where $x^{(i)}$ denotes the i^{th} sample in the training set. The second term is the regularization which we take the limit so the solution is unique (pseudo inverse solution) for an overparameterized setup ($n < p$).

C.1 Eigenfunctions - orthonormalized features

In many cases, $[\Phi_1(x), \Phi_2(x), \dots, \Phi_p(x)]$ are not orthonormal. For example, the features $[x, x^2]$ of $f(x) = w_1 x + w_2 x^2$ for $q = \text{unif}[0, 1]$ are not orthonormal:

$$\langle x|x^2 \rangle = \int_0^1 x^3 dx \neq 0, \quad \langle x|x \rangle = \int_0^1 x^2 dx \neq 1, \quad \langle x^2|x^2 \rangle = \int_0^1 x^4 dx \neq 1. \quad (12)$$

The diagonalization into the eigenfunctions returns the orthonormal basis of the hypothesis (Hilbert) space $\mathcal{H} = \text{span}\{\Phi_1(x), \Phi_2(x), \dots, \Phi_p(x)\}$, more formally known as Reproducing Kernel Hilbert Space (RKHS). The eigenvalue now shows the norm of the feature along the direction of eigenfunction as the features $[\Phi_1(x), \Phi_2(x), \dots, \Phi_p(x)]$ are not normalized (Fig. 8).

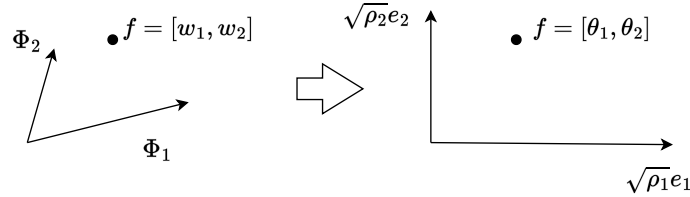


Figure 8: **Diagonalization of features** Since the features $[\Phi_1(x), \Phi_2(x), \dots, \Phi_p(x)]$ span a vector space, each function $\Phi_k : \mathcal{X} \rightarrow \mathbb{R}$ can be represented as a vector. The overlap among Φ_k 's (non-zero linear correlation) and differing norms of Φ_k 's result in diagonalized features $[\sqrt{\rho_1}e_1, \sqrt{\rho_2}e_2, \dots, \sqrt{\rho_p}e_p]$ to have distinct intensities (norms) ρ_1, \dots, ρ_p .

The transformation between the eigenfunction basis and the feature basis is

$$\Phi_i(x) = \sum_j O_{ij} \sqrt{\rho_j} e_j(x), \quad O_{ij} = \frac{1}{\sqrt{\rho_j}} \langle \Phi_i | e_j \rangle, \quad (13)$$

where $O \in \mathbb{R}^{p \times p}$ is an orthogonal matrix (follows trivially from Eq. (2)). Using Eq. (13), the model can be reparameterized in the eigenfunction basis

$$f(x) = \sum_{k=1}^p w_k \Phi_k(x) = \sum_{k=1}^p \theta_k \sqrt{\rho_k} e_k(x). \quad (14)$$

Note that because $\theta = Ow$, the norm of the parameters is conserved (i.e. $\|\theta\|_F = \|w\|_F$), indicating that weighted basis $[\sqrt{\rho_1}e_1, \sqrt{\rho_2}e_2, \dots, \sqrt{\rho_p}e_p]$ instead of normalized basis $[e_1, e_2, \dots, e_p]$ must be used to represent the ‘intensity’ or norm of the features $[\Phi_1(x), \dots, \Phi_p(x)]$.

C.2 Inductive bias toward large features for minimum norm solution

For overparameterized linear models, the inductive bias determines the returned function as many functions can express the training set. Here, we brief the linear models' inductive bias toward larger (significant) features or eigenfunctions [16–21, 54].

The inductive bias is quantified through learnability L_k [54] or the expectation ratio between the learned coefficient and true coefficient for e_k :

$$L_k := \mathbf{E}_{S \sim q^n} \left[\frac{\langle \hat{f} | e_k \rangle}{\langle f^* | e_k \rangle} \right] = \frac{\rho_k}{\rho_k + \kappa}, \quad \text{where } \sum_{k=1}^p \frac{\rho_k}{\rho_k + \kappa} = n. \quad (15)$$

The learnabilities always sum to n — the number of training datapoints — and constant κ is the constant that satisfies the equality.

We can understand the inductive bias from the (vanishing) regularization on L^2 norm ($\lambda \|w\|_F^2$ in Eq. (11)) and parameterization in Eq. (14). If different eigenfunctions can equally express the training set, eigenfunction with larger eigenvalue often requires smaller coefficient θ_k to express the samples. Because $\|w\|_F^2 = \|\theta\|_F^2$, expressing the data with larger (eigenvalue) eigenfunctions minimizes the norm, creating an inductive bias toward larger features.

Instead of the derivation found in the references [16–21] — which requires random matrix theory or replica trick — we show an example of the inductive bias in Fig. 9.

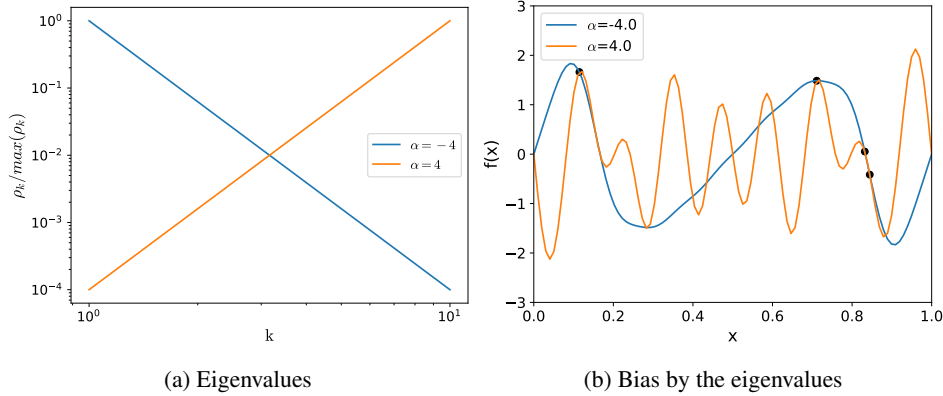


Figure 9: **Different inductive biases by the eigenvalues (intensity).** Two 10-parameter linear models are trained on 4 datapoints (overparameterized) with gradient flow. Both linear models use sin basis functions such that $f(x) = \sum_k^{10} w_k k^\alpha \sqrt{2} \sin(2\pi kx)$ — spanning an identical function space — but differ in the eigenvalues with $\alpha = -4$ (blue) and $\alpha = 4$ (orange), leading to different inductive biases. **(a):** The blue model has a greater intensity for lower-frequency sin functions, while the orange model shows the opposite. **(b):** The learned functions show that the blue model used lower-frequency functions while the orange used higher-frequency functions to express the training samples.

Fig. 9 shows that two linear models with same hypothesis space but different eigenvalues learn dramatically different functions. The blue model has large eigenvalues for low-frequency functions and fits the datapoints using low-frequency functions. The orange model with opposite eigenvalue distribution fits the training set with high-frequency functions — a clear example of an inductive bias toward large (intensity) features.

In the references, the generalization loss is

$$\mathcal{L}_G = \frac{1}{1 - \frac{1}{n} \sum_j^p L_j^2} \left(\sum_k^p (1 - L_k)^2 \langle e_k | f^* \rangle^2 \right). \quad (16)$$

The equation formalizes the task-model alignment: the alignment between large features (large ρ_k thus large L_k) and high quality (large $\langle e_k | f^* \rangle$) leads to better generalization.

C.3 Dynamical inductive bias toward large features

Here, we review how gradient descent introduces the dynamical inductive bias toward larger features. For a linear model with feature map Φ and kernel integral operator \mathcal{T} , the gradient flow dynamics under MSE loss with infinite training datapoints and zero initialization becomes

$$\frac{df}{dt} = -\mathcal{T}[f - f^*]. \quad (17)$$

The derivation is trivial with

$$\frac{df}{dt}(x') = \sum_k^p \frac{dw_k}{dt} \Phi_k(x') = \sum_k^p -\frac{\partial \mathcal{L}}{\partial w_k} \Phi_k(x') \quad (18)$$

$$= -\mathbf{E}_x \left[(f(x) - f^*(x)) \sum_k^p \frac{df}{dw_k}(x) \right] \Phi_k(x') \quad (19)$$

$$= -\mathbf{E}_x \left[(f(x) - f^*(x)) \sum_k^p \Phi_k(x) \right] \Phi_k(x') \quad (20)$$

$$= -\mathcal{T}[f - f^*], \quad (21)$$

where in the second line, we used Eq. (11) on infinite datapoints so $\mathcal{L}_{emp} = \mathcal{L}$. In the last line, we used the definition of integral operator (Eq. (1)).

Using the eigenvalues ρ_k and eigenfunctions e_k of the kernel integral operator \mathcal{T} , we obtain the dynamics for each $\langle e_k | f \rangle$ by inner producting e_k on both sides of Eq. (17),

$$\frac{d\langle e_k | f \rangle}{dt} = \mathbf{E}_{x'} \left[e_k(x') \frac{df}{dt}(x') \right] = -\mathbf{E}_{x'} [e_k(x') \mathcal{T}[f - f^*](x')] \quad (22)$$

$$= -\langle e_k | \mathcal{T}[f - f^*] \rangle \quad (23)$$

$$= -\rho_k (\langle e_k | f \rangle - \langle e_k | f^* \rangle), \quad (24)$$

where we use the definition of eigenfunction in the last line (Eq. (2)). Expanding f in the eigenfunction basis and plugging in Eq. (22), the function f at time t is a sum of p independent modes that saturate faster for larger eigenvalues:

$$f(x)|_t = \sum_{k=1}^p \langle e_k | f^* \rangle (1 - e^{-\rho_k t}) e_k(x), \quad (25)$$

where we assumed f is a zero function at initialization. Eq. (25) shows that gradient flow decouples the dynamics of linear models into p modes, where each mode corresponds to the evolution of $\langle e_k | f \rangle$ having a saturation speed governed by ρ_k — thus the dynamical inductive bias toward larger eigenfunction.

C.4 Application to our method

Here, we detail the intuition of our visualization methods. As described in Bengio et al.[1], feature learning (of representation) is providing **better** features for a simpler learner. The analogy allows us to describe a neural network as (1) feature map Φ providing better features for (2) the last layer — the simple learner (Fig. 10). Yet, **better** features for the last layer is ill-defined.

The last layer interacts with rest of the network only through the features. While the exact dynamics differs from linear models, the last layer maintains the dynamical inductive bias (Appendix C.3) toward larger features. Furthermore, the quality ($\langle e_k | f^* \rangle$), utilization ($\langle e_k | \hat{f} \rangle$), and intensity ρ_k formalisms readily extend to the last layer features, motivating our visualization method.

In the rich regime, features evolve during training, and Fig. 11(a-c) demonstrates an example of change in features for 4-layer MLP trained to fit the Heaviside step function. The eigenfunctions are difficult to visualize in practice as the input space is high dimensional. Fig. 11(d-f) shows our visualization, capturing the evolution of features by measuring properties natural to linear regression.

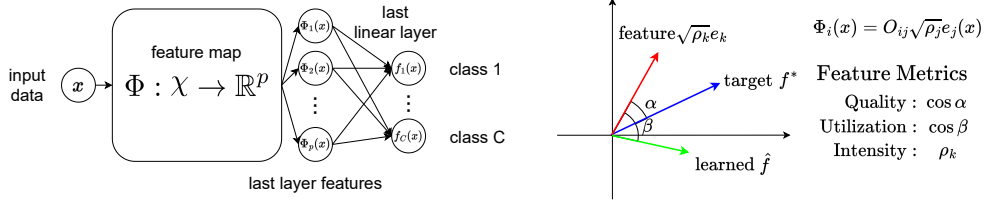


Figure 10: **A neural network decomposed into a feature map and a linear last layer. (left):** An abstract diagram depicting a DNN architecture as a combination of the feature map $\Phi : \mathcal{X} \rightarrow \mathbb{R}^p$ from the input space \mathcal{X} to the p post activations of the penultimate layer, and final linear classifier for C -way classification. Most neural networks share this abstract structure and mainly vary in how they create their feature maps. **(right):** Illustration of the visualization methods in function space.

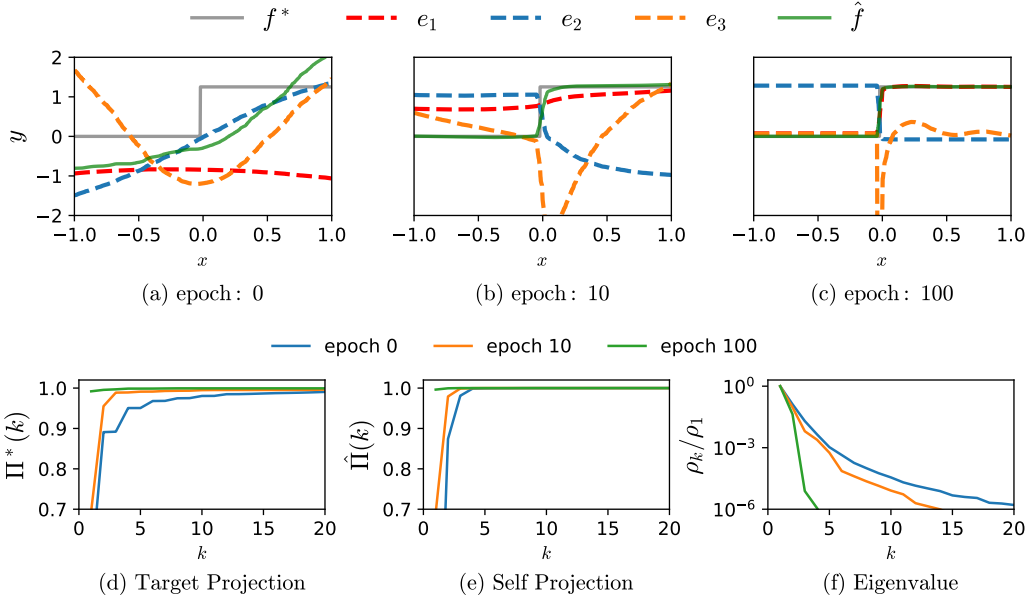


Figure 11: **Toy model demonstrating feature learning.** A 4-layer MLP with width 1000 and scalar input and output is trained to learn the Heaviside step function f^* over the domain $[-1, 1]$. **(a):** The first three eigenfunctions (dashed) are shown at initialization, resembling orthogonal polynomials. **(b,c):** During training, features evolve such that a single feature (red) fits both the target and learned functions (grey and green). **(d,e,f):** Our visualization metrics defined in Eq. (5) at different epochs. (d) and (e) show that fewer features can express the target/learned function, and (f) shows that only a few features are significant after training.

D The relationship between the MP-operator \mathcal{T}_{MP} and neural collapse

Neural collapse [6] (NC) refers to a state of a DNN when the feature vectors of the training set and last layer weights form a symmetric and clustered structure at the terminal phase of training (TPT) or when trained past the point where the training error vanishes. The structure has been studied mainly in the Unconstrained Feature Model (UFM) [5] and has sparked theoretical studies. See Kothapalli et al. [35] for a review.

NC is defined by the emergence of four interconnected phenomena upon TPT: NC1) collapse of within-class variability, NC2) convergence of features to a rigid simplex equiangular tight frame (ETF) structure, NC3) alignment of the last layer and features, and NC4) simplified decision by nearest class:

1. Within class variance tends to 0

$$\Sigma_W \Sigma_b^\dagger \rightarrow 0, \quad (26)$$

2. Convergence to simplex ETF

$$\frac{(\mu_i - \bar{\mu})^T (\mu_j - \bar{\mu})}{\|(\mu_i - \bar{\mu})\|_2 \|(\mu_j - \bar{\mu})\|_2} \rightarrow \frac{C \delta_{ij} - 1}{C - 1}, \quad (27)$$

3. Convergence to self duality

$$\frac{w_i}{\|w_i\|_2} - \frac{\mu_i - \bar{\mu}}{\|(\mu_i - \bar{\mu})\|_2} \rightarrow 0, \quad (28)$$

4. Simplification to nearest class center

$$\arg \max_i w_i \Phi(x) + b_i \rightarrow \arg \min_i \|\Phi(x) - \mu_i\|_2. \quad (29)$$

D.1 Proofs of proposition 1 and 2

For completeness, we restate the conditions. We assume the true distribution q equals the empirical distribution of the training set — the expectation \mathbf{E}_x (and bra-ket notation) is over the training samples. We assume balanced classification and define A_i as the set of training samples with class label i . We assume the learned function is a perfectly classifying indicator function, giving

$$\hat{f}_i(x) := \begin{cases} 0 & : x \notin A_i \\ 1 & : x \in A_i \end{cases} \quad (30)$$

The feature class mean vector for label i is

$$\mu_i = \mathbf{E}_{x \in A_i} [\Phi(x)] = \frac{C}{n} \sum_{x \in A_i} \Phi(x) = C \langle \hat{f}_i | \Phi \rangle. \quad (31)$$

Note that $\langle \hat{f}_i | \Phi \rangle \in \mathbb{R}^p$ is a vector with $\langle \hat{f}_i | \Phi \rangle = [\langle \hat{f}_i | \Phi_1 \rangle, \dots, \langle \hat{f}_i | \Phi_p \rangle]$.

The global mean vector is

$$\bar{\mu} = \frac{1}{C} \sum_i^C \mu_i = \langle \Phi | \sum_{i=1}^C \hat{f}_i \rangle = \langle \mathbf{1} | \Phi \rangle. \quad (32)$$

The feature intra (within)-class covariance $\Sigma_W \in \mathbb{R}^{p \times p}$ is

$$\Sigma_W := \sum_i^C \mathbf{E}_{x \in A_i} [(\Phi(x) - \mu_i)(\Phi(x) - \mu_i)^T]. \quad (33)$$

The feature inter (between)-class covariance $\Sigma_b \in \mathbb{R}^{p \times p}$ is

$$\Sigma_b := \frac{1}{C} \sum_i^C (\mu_i - \bar{\mu})(\mu_i - \bar{\mu})^T. \quad (34)$$

Lemma 1. For the conditions given above, if $\mathcal{T}[f](x') = \Phi(x')^T \mathbf{E}_{x \sim q'} [\Phi(x)f(x)]$ is \mathcal{T}_{MP} , then

$$\Phi^T(x')^T(\mu_i - \bar{\mu}) = a_2(C\hat{f}_i(x') - 1). \quad (35)$$

Proof. By the definition of indicator functions of equal partitions,

$$\langle \hat{f}_i | \hat{f}_j \rangle = \frac{1}{C} \delta_{ij}, \quad \sum_{i=1}^C \hat{f}_i = \mathbf{1}, \quad \langle \mathbf{1} | \hat{f}_j \rangle = \frac{1}{C}. \quad (36)$$

It follows that $C\hat{f}_j - \mathbf{1}$ is orthogonal to $\mathbf{1}$:

$$\langle \mathbf{1} | C\hat{f}_i - \mathbf{1} \rangle = 0. \quad (37)$$

We can express the function $\Phi(x')^T(\mu_i - \bar{\mu}) : \mathcal{X} \rightarrow \mathbb{R}$ in terms of \mathcal{T}

$$\Phi(x')^T(\mu_i - \bar{\mu}) = \Phi(x')^T \left(\langle \Phi | C\hat{f}_i \rangle - \langle \Phi | \mathbf{1} \rangle \right) \quad (38)$$

$$= \Phi(x')^T \mathbf{E}_x [\Phi(x)(C\hat{f}_i(x) - 1)] \quad (39)$$

$$= \mathcal{T}[C\hat{f}_i - 1](x'), \quad (40)$$

where we used the definition of the means (Eqs. (31) and (32)) in the first line and the definition of \mathcal{T} (Eq. (1)) in the last line. As \mathcal{T} is \mathcal{T}_{MP} , we obtain

$$\Phi(x')^T(\mu_i - \bar{\mu}) = \mathcal{T}_{MP}[C\hat{f}_i - 1](x') \quad (41)$$

$$= a_2(C\hat{f}_i(x') - 1), \quad (42)$$

where we used Eq. (37) and the definition of \mathcal{T}_{MP} (Definition 1). \square

Corollary 1. In the setup of Lemma 1, we have

$$\mu_i^T(\mu_j - \bar{\mu}) = a_2(C\delta_{ij} - 1).$$

Proof. From the definition of class mean (Eq. (31)) and Lemma 1,

$$\mu_j^T(\mu_i - \bar{\mu}) = \mathbf{E}_{x'} [C\hat{f}_j(x')\Phi(x')^T(\mu_i - \bar{\mu})] \quad (43)$$

$$= \mathbf{E}_{x'} [C\hat{f}_j(x')a_2(C\hat{f}_i(x') - 1)] \quad (44)$$

$$= a_2(C\delta_{ij} - 1), \quad (45)$$

where we used that $\mathbf{E}_{x'}[\hat{f}_j^2(x')] = \mathbf{E}_{x'}[\hat{f}_j(x')] = C^{-1}$. \square

Proposition 1. If \mathcal{T} is an MP-operator, then the NCI condition (collapse of within-class variability) $\Sigma_b^\dagger \Sigma_W = 0$ holds, where inter-class covariance matrix Σ_b and intra-class covariance matrix Σ_W are

$$\Sigma_b = \sum_{j=1}^C (\mu_j - \bar{\mu})(\mu_j - \bar{\mu})^T \quad \text{and} \quad \Sigma_W = \sum_{i=1}^C \mathbf{E}_{x \in A_i} [(\Phi(x) - \mu_i)(\Phi(x) - \mu_i)^T].$$

Proof. We will show that $\text{Tr}(\Sigma_b \Sigma_W) = 0$, which automatically proves the proposition as covariance matrices are positive semi-definite. We have

$$\text{Tr}(\Sigma_b \Sigma_W) = \text{Tr} \left(\sum_j (\mu_j - \bar{\mu})(\mu_j - \bar{\mu})^T \sum_i \mathbf{E}_{x \in A_i} (\Phi(x) - \mu_i)(\Phi(x) - \mu_i)^T \right) \quad (46)$$

$$= \sum_{i,j} \mathbf{E}_{x \in A_i} \left[((\Phi(x) - \mu_i)^T (\mu_j - \bar{\mu}))^2 \right] \quad (47)$$

$$= \sum_{i,j} \mathbf{E}_{x \in A_i} \left[a_2^2 \left(C\hat{f}_j(x) - 1 - C\delta_{ij} + 1 \right)^2 \right] \quad (48)$$

$$= a_2^2 C^2 \sum_{i,j} \mathbf{E}_{x \in A_i} \left[\left(\hat{f}_j(x) - \delta_{ij} \right)^2 \right], \quad (49)$$

where we used linearity of trace, sum, expectation in the first line and Lemma 1 in the second line. Expanding Eq. (49),

$$\text{Tr}(\Sigma_b \Sigma_W) = a_2^2 C^2 \sum_{i,j} \mathbf{E}_{x \in A_i} \left[(1 - 2\delta_{ij}) \hat{f}_j(x) + \delta_{ij} \right] \quad (50)$$

$$= a_2^2 C \sum_{i,j} (\delta_{ij} (2 - 2\delta_{ij})) \quad (51)$$

$$= 0, \quad (52)$$

where we used that learned functions are indicator functions in the second line. \square

Proposition 2. *If \mathcal{T} is an MP-operator, then the NC2 condition (convergence of features to a simplex equiangular tight frame) holds:*

$$(\mu_i - \bar{\mu})^T (\mu_j - \bar{\mu}) \propto \delta_{ij} - \frac{1}{C}.$$

Proof. From the definition of global mean (Eq. (32)) and Lemma 1,

$$\bar{\mu}^T (\mu_i - \bar{\mu}) = \mathbf{E}_{x'} [\Phi(x')^T (\mu_i - \bar{\mu})] \quad (53)$$

$$= \mathbf{E}_{x'} [a_2 (C \hat{f}_i(x') - 1)] \quad (54)$$

$$= 0. \quad (55)$$

Using Corollary 1 and Eq. (55),

$$(\mu_i - \bar{\mu})^T (\mu_j - \bar{\mu}) = C a_2 (\delta_{ij} - \frac{1}{C}). \quad (56)$$

\square

D.2 The first eigenfunction, the constant function, the analog of global mean vector in simplex ETF

Here, we discuss the constant function, which, by definition of \mathcal{T}_{MP} (Definition 1), is the largest eigenfunction if \mathcal{T} is \mathcal{T}_{MP} . In all experiments except Fig. 11, the largest eigenfunction is the constant function throughout training, with $\langle \mathbf{1} | e_1 \rangle > 0.95$. For our visualization, we ignore the first eigenvalue from analysis as the constant function is removed in CKA (Eq. (7)).

In the NC2 condition, the k -simplex ETF structure is a set of k orthogonal vectors projected on $k - 1$ dimensional space along the complement of the global mean vector. For example, projecting $[0, 0, 1]$, $[0, 1, 0]$, and $[1, 0, 0]$ onto the orthogonal complement of $[\frac{1}{3}, \frac{1}{3}, \frac{1}{3}]$ (the global mean vector) gives three vertices $[-\frac{1}{3}, -\frac{1}{3}, \frac{2}{3}]$, $[-\frac{1}{3}, \frac{2}{3}, -\frac{1}{3}]$, $[\frac{2}{3}, -\frac{1}{3}, -\frac{2}{3}]$ which forms an (ordinary plane) equilateral triangle.

Our operator \mathcal{T}_{MP} (Definition 1) has an analogous structure, where it is a (scaled) projection operator ($a_2 P_{\hat{H}}$) except along the constant function. The CKA (Eq. (7)) also measures the alignment except along the mean direction (for matrices) or the constant direction (for operators). This allows neural networks to have any arbitrary eigenvalue for the constant function, yet perfectly align with $\mathcal{D}_{LR} = 0$.

When \mathcal{T} is \mathcal{T}_{MP} , the definition of \mathcal{T}_{MP} (Definition 1) trivially shows that the largest eigenfunction is the constant function. A peculiar observation is that the first eigenfunction of \mathcal{T} remains the constant function ($\langle \mathbf{1} | e_1 \rangle > 0.95$) **throughout training** in all our experiments (except Fig. 11). This pattern also appears in hierarchical datasets [55], suggesting that natural data may consistently prioritize the constant function as the dominant mode — warranting further investigation.

D.3 Generality of our metric beyond neural collapse

As discussed in the main text, our metrics are defined in terms of functions (random variables) while neural collapse is defined by the feature vectors of the training set. Working in the function space, we can measure the quality Eq. (5), which is inaccessible from formalism using training feature vectors.

Another important difference is that we focus on the learned function instead of mean class label vectors. This allows more independence beyond neural collapse, allowing the framework to be applied on broader set of tasks: tasks with orthogonal and isotropic target functions form a broader class than balanced classification tasks. Regression task with scalar output is an example.

In Fig. 12, we train ResNet18 on MNIST as a **regression** task with scalar output ($f^* : \mathcal{X} \rightarrow \mathbb{R}$), where a digit i is correctly predicted if $i - 0.5 < f(x) < i + 0.5$. Unlike C -way classification, which typically uses C features, the regression model reaches the rich regime with just two — one of which is constant. Neural collapse formalism, focusing on class labels, does not readily extend to regression tasks, demonstrating that our function-based formalism is more general, label-independent, and applicable beyond classification.

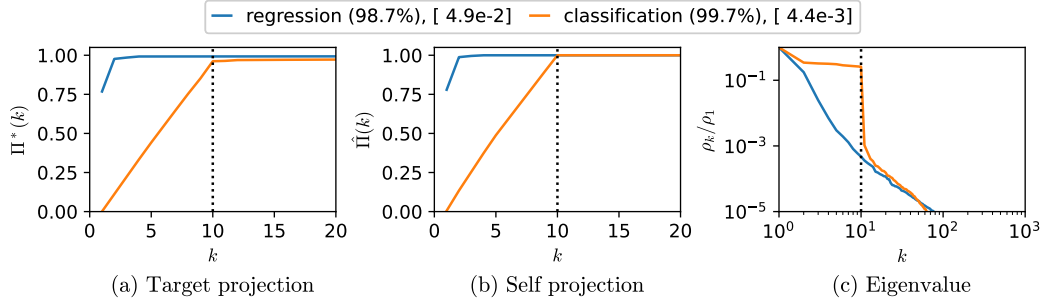


Figure 12: **Rich dynamics for regression problem with scalar output.** ResNet18 was trained on MNIST via regression (blue) and classification (orange). For regression, the target/learned functions are scalar output functions, and an image x with digit i is correctly classified if $i - 0.5 < f(x) < i + 0.5$. It can be seen that both models are in the rich regime, using the minimum number of features.

Finally, the independence from the class labels allows another benefit of being applicable during training. Neural collapse is defined only during the terminal stage of training and assumes 100% classification. A measure without perfect classification can lead to unstable values, typically rising from the pseudo-inverse of Σ_b (See also Appendix F). The NC1 measure shows a dramatic change in logarithmic scale for experiments in Fig. 2(a,b) while our measure is more robust to such differences.

E Examples of our visualization framework

In this section, we report additional findings made with our visualization tools.

Rich dynamics \neq generalization. In Fig. 1, we showed an example where rich dynamics led to poorer performance. Fig. 13 shows a similar experiment in which both rich and lazy models achieve near-perfect performance ($> 95\%$ test accuracy). Our visualization clearly shows the different usages of features even when the performances are similar.

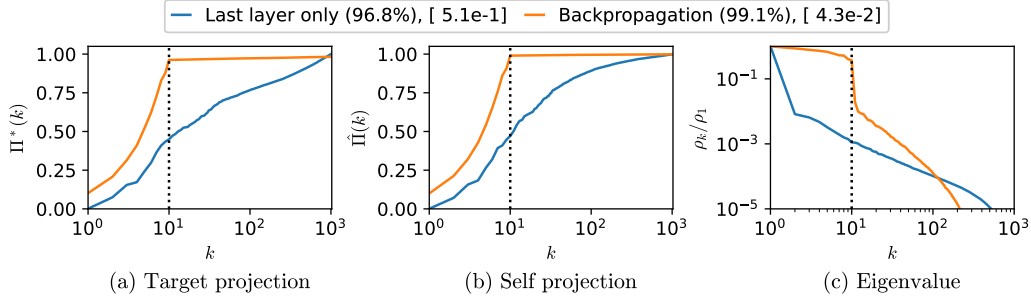


Figure 13: **Generalization does not imply rich regime.** A CNN with width $p = 1024$ is trained on the full MNIST dataset using two dynamics: last-layer-only training (lazy) and full backpropagation (rich). Although both dynamics achieve test accuracy above 95%, they lead to dramatically different use/significance of features: the metrics concentrate on the first 10 features for the rich regime, and they are more evenly spread for the lazy regime.

Low rank bias. Table 1 shows that low-rank inductive bias is strong in vision tasks, where the number of significant features always equals C (the number of orthogonal functions). See Eq. (9) in Appendix B.4 for the $D_{eff}(\rho)$ expression. We also observe that our measure \mathcal{D}_{LR} is small in these setups.

Table 1: Metrics of ResNet18 and VGG16 trained on image datasets

model	dataset	$D_{eff}(\rho)$	$D_{eff}(\hat{Q})$	\mathcal{D}_{LR}	test accuracy (%)
ResNet18	MNIST	10.1	10.0	$4.4 \cdot 10^{-3}$	99.7
VGG16	MNIST	10.0	10.0	$1.8 \cdot 10^{-2}$	99.4
ResNet18	CIFAR10	10.4	10.0	$3.1 \cdot 10^{-3}$	94.8
VGG16	CIFAR10	10.0	10.0	$1.1 \cdot 10^{-3}$	93.3
ResNet18	CIFAR100	99.9	99.7	$2.5 \cdot 10^{-2}$	78.3
VGG16	CIFAR100	95.8	99.4	$7.4 \cdot 10^{-2}$	71.9

Weight decay is not the source of inductive bias. Fig. 14 shows that weight decay indeed aids low-rank representation and smaller \mathcal{D}_{LR} . However, the model without any weight decay already shows sufficiently low-rank representations, suggesting that dynamical inductive bias, not the weight decay is the main driving cause of low-rank representations.

Effect of learning rate on rich dynamics. Fig. 15 shows that a smaller learning rate induces lazier dynamics, while a too large learning rate (largest without gradient blow up) also deviates from the rich regime. The optimal learning rate correlates with the best performance and the richest dynamics. However, no extensive searches were performed on learning rates.

Role of architecture. As studied in Saxe et al. [55], the architecture and dataset pair can influence the performance even when dynamics are greedy (race toward shared representation). In Fig. 16, we examine the dynamics of ResNet18 and a 4-layer MLP trained on CIFAR-10. In Fig. 16(a), the training dynamics is restricted to the first 10 significant features, consistent with theoretical work in

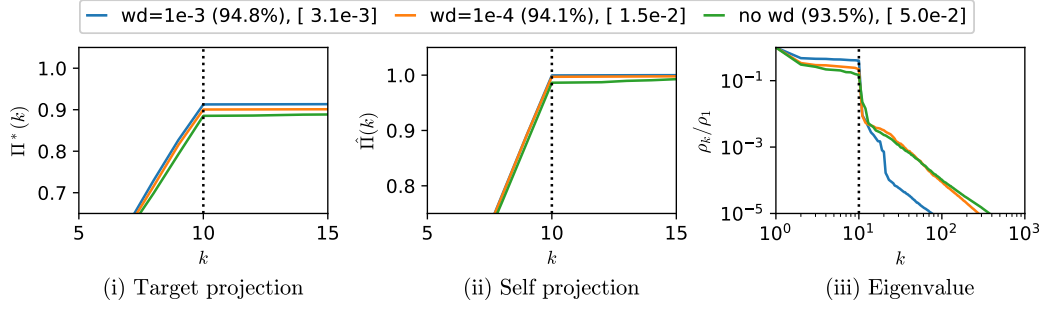


Figure 14: **Effect of weight decay on rich dynamics.** ResNet18 trained on CIFAR10 with varying weight-decay (shown relative value to the fixed learning rate of 0.05). Larger weight decay leads to richer dynamics with smaller \mathcal{D}_{LR} , but the dynamics is already rich without the weight decay.

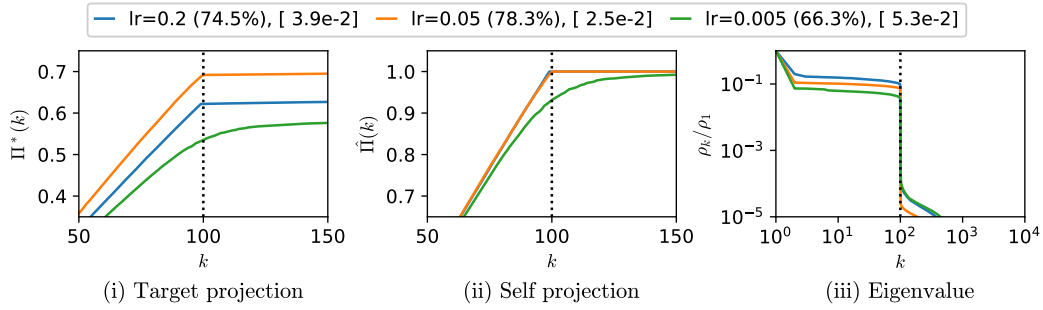


Figure 15: **Effects of learning rates on feature learning and generalization.** We explore the effect of changing the learning rate for a ResNet18 on CIFAR100. Note that a lower learning rate leads to a lazier regime and poorer performance. The best performance is for the intermediate learning rate in the rich regime with the tightest \mathcal{D}_{LR} measure.

linear neural networks. In Fig. 16(b), the training is mainly focused on the first 10 features, but we observe that more features are used as training progresses, more similar to the dynamics of linear models. We speculate that the lack of ability to feature learn in the earlier layers leads to the use of additional features and thus leads to lazier training dynamics.

Cross entropy loss. Fig. 17 shows that our method extends to models trained on cross-entropy loss, while the mathematical interpretation is less straightforward.

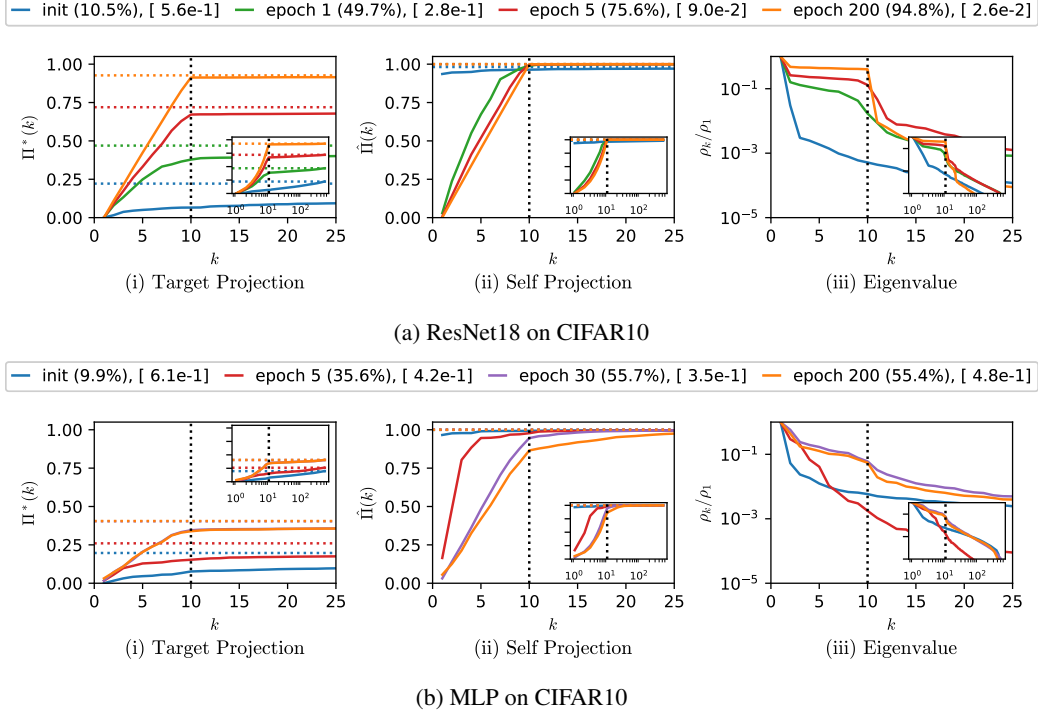


Figure 16: **Role of architecture in the richness of the dynamics.** ResNet18 (a) and a 4-layer MLP of width 512 (b) are trained on CIFAR10, and their metrics are shown at different epochs. ResNet18 concentrates the metrics on the first 10 features after just one epoch, which persists until the end of training. In contrast, MLP shows a less dramatic concentration on the first 10 features and deviates from the rich dynamics around epoch 30 when it begins to use more features. Insets display all 512 features rather than just the top 25.

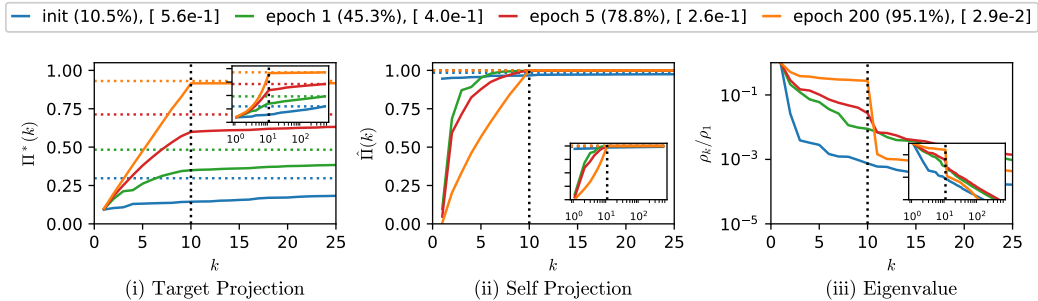


Figure 17: **Training with cross-entropy loss.** We apply our visualization method to a ResNet18 trained on CIFAR-10 with cross-entropy loss. Similar to the MSE-trained model, it achieves small value of \mathcal{D}_{LR} and shows concentration of feature usage and significance. Insets display all 512 features rather than just the top 25.

F Empirical details

Here, we share information on our practical setups and their statistical significance.

F.1 Statistical significance

We reproduce tables from the main text but with the addition of one standard deviation values. In the main text, all error bars in the plots represent one standard deviation over at least three runs.

Table 2: Statistical significance of Figure 1(b)

	Full backprop (Rich)	Last layer only (Lazy)
Train acc. \uparrow	100 (± 0)%	98.7 (± 0.11) %
Test acc. \uparrow	10.0 ($\pm 4.3 \cdot 10^{-2}$)%	74.4 (± 0.19) %
$\mathcal{D}_{LR} \downarrow$	$8.7 \cdot 10^{-3}$ ($\pm 4.0 \cdot 10^{-4}$)	$6.3 \cdot 10^{-1}$ ($\pm 3.2 \cdot 10^{-3}$)

Table 3: Statistical significance of Figure 2(a)

Epoch	0 (init)	200
Train Acc. \uparrow	10.0 (± 0.8)%	10.2(± 0.27)%
Test Acc. \uparrow	9.85 (± 1.0)%	10.0(± 0.33)%
$\mathcal{D}_{LR} \downarrow$	0.59 ($\pm 1.6 \cdot 10^{-2}$)	1.0 ($\pm 6.4 \cdot 10^{-5}$)
$\mathcal{S}_{init} \downarrow$	1.0 (± 0)	0.20 ($\pm 1.1 \cdot 10^{-2}$)
$\ \theta\ _F^2 \downarrow$	$3.1 \cdot 10^3$ ($\pm 3.5 \cdot 10^2$)	$2.2 \cdot 10^{-5}$ ($\pm 2.5 \cdot 10^{-9}$)
NC1 \downarrow	$1.2 \cdot 10^5$ ($\pm 7.2 \cdot 10^2$)	$7.5 \cdot 10^{-14}$ ($\pm 1.5 \cdot 10^{-14}$)
$Tr(\Sigma_W) \downarrow$	15.6 (± 1.4)	$7.1 \cdot 10^{-18}$ ($\pm 1.1 \cdot 10^{-18}$)

Table 4: Statistical significance of Figure 2(b)

α	$2 \cdot 10^{-1}$	$2 \cdot 10^0$	$2 \cdot 10^1$
Train Acc. \uparrow	100 (± 0)%	100 (± 0)%	100 (± 0)%
Test Acc. \uparrow	92.7 ($\pm 3.4 \cdot 10^{-2}$)%	92.4 ($\pm 5.2 \cdot 10^{-2}$)%	88.3 ($\pm 3.7 \cdot 10^{-1}$)%
$\mathcal{D}_{LR} \downarrow$	$4.9 \cdot 10^{-2}$ ($\pm 4.4 \cdot 10^{-3}$)	$1.1 \cdot 10^{-1}$ ($\pm 9.4 \cdot 10^{-3}$)	$5.6 \cdot 10^{-1}$ ($\pm 6.1 \cdot 10^{-2}$)
$\mathcal{S}_{init} \downarrow$	$6.8 \cdot 10^{-2}$ ($\pm 2.1 \cdot 10^{-3}$)	$4.1 \cdot 10^{-2}$ ($\pm 4.5 \cdot 10^{-3}$)	$5.2 \cdot 10^{-2}$ ($\pm 1.8 \cdot 10^{-2}$)
$\ \theta\ _F^2 \downarrow$	$3.4 \cdot 10^3$ ($\pm 1.1 \cdot 10^1$)	$3.2 \cdot 10^3$ (± 4.4)	$3.2 \cdot 10^3$ (± 2.0)
NC1 \downarrow	$2.3 \cdot 10^4$ ($\pm 4.1 \cdot 10^3$)	$3.2 \cdot 10^3$ ($\pm 4.3 \cdot 10^2$)	$8.1 \cdot 10^2$ ($\pm 1.4 \cdot 10^2$)
$Tr(\Sigma_W) \downarrow$	2.0 (± 0.25)	$3.1 \cdot 10^{-1}$ ($\pm 2.3 \cdot 10^{-2}$)	$1.2 \cdot 10^{-1}$ ($\pm 1.2 \cdot 10^{-2}$)

F.2 Discussion on NC1 measure

In Tables 3 and 4, the NC1 measure is numerically unstable due to the pseudo-inverse of Σ_b . For stability, We used $\Sigma_b^\dagger \approx (\Sigma_b + 10^{-4}I)^\dagger$. In addition to NC1, we consider a similar measure $Tr(\Sigma_W)$ [6] for collapse of within class variability, which is also reported in Tables 3 and 4. The measure $Tr(\Sigma_W)$ also shows a similar trend to NC1.

F.3 Dataset details

We use publicly available datasets, including MNIST [56] and CIFAR-10/100 [57] from Pytorch [58], and mod p division task from <https://github.com/teddykoker/grokking>.

F.4 Model details

Our model implementations are based on publicly available code assets, including VGG16 from PyTorch [58], ResNet18 from Nakkiran et al. [59], and the modular division task from <https://github.com/teddykoker/grokking>.

As described in the main text, we only trained our models on MSE loss where the targets are one-hot vectors (up to scaling constant). The constant α is used to scale the output $y \rightarrow y/\alpha$.

Table 5: Dataset details

Figure	dataset	training sample count	α	batch size
Fig. 1	Encoded MNIST (Appendix F.4.1)	60,000 (all)	1/3	128
Fig. 2(a)	MNIST	60,000 (all)	1	128
Fig. 2(b,c)	MNIST	1,000	.	128
Fig. 3	CIFAR-10	10,000	1/3	128
Fig. 4	mod-p division	4,656	1	512
Fig. 5	CIFAR-10	.	1/3	128
Fig. 6	CIFAR-100	50,000 (all)	1/10	128
Fig. 7	CIFAR-100	50,000 (all)	1/10	128

F.4.1 Encoded MNIST

In Fig. 1, we encoded the labels as one-hot vectors on the first 10 pixels of the MNIST dataset. For the training set, we encoded the true labels, but for the test set, we encoded random labels.

F.4.2 CIFAR-10/100

For CIFAR-10/100, we use standard augmentation using randomcrop 32 with padding 4 and random horizontal flip with probability 0.5. We also use standard normalization with mean [0.4914, 0.4822, 0.4465] and standard deviation [0.2023, 0.1994, 0.2010] for each channels.

Table 6: Training details

Figure	optimizer	learning rate	momentum / beta	weight decay	epochs	learning rate scheduling
Fig. 1	Adam	$1 \cdot 10^{-3}$	[0.9, 0.999]	0	100	None
Fig. 2(a)	SGD	$1 \cdot 10^{-6}$	0	$1 \cdot 10^{-3}$	200	None
Fig. 2(b,c)	Adam	$1 \cdot 10^{-3}$	[0.9, 0.999]	0	100	None
Fig. 3	SGD	$5 \cdot 10^{-2}$	0.9	$5 \cdot 10^{-5}$	200	$\times 0.2$ per 60 epochs
Fig. 4	Adam	$1 \cdot 10^{-3}$	[0.9, 0.98]	0	4000	None
Fig. 5	SGD	$5 \cdot 10^{-2}$	0.9	$5 \cdot 10^{-5}$	200	$\times 0.2$ per 60 epochs
Fig. 6	SGD	$1 \cdot 10^{-2}$	0.9	$1 \cdot 10^{-5}$	400	None
Fig. 7	SGD	$5 \cdot 10^{-2}$	0.9	$5 \cdot 10^{-5}$	400	$\times 0.2$ per 60 epochs

F.5 Compute resources

The models ran on GPU cluster containing RTX 1080 (8GB), RTX 2080 (8GB), RTX3060 (12 GB), and RTX3090 (24GB). The typical time to train a model is 2 hours, but it varies from 10 minutes to 6 hours depending on the experiment. The evaluation metrics take less than 5 minutes and may need up to 2GB of CPU memory.